

Quasars as probes of cosmological reionization

Daniel J. Mortlock

Abstract Quasars are the most luminous non-transient sources in the epoch of cosmological reionization (i.e., which ended a billion years after the Big Bang, corresponding to a redshift of $z \simeq 5$), and are powerful probes of the inter-galactic medium at that time. This review covers current efforts to identify high-redshift quasars and how they have been used to constrain the reionization history. This includes a full description of the various processes by which neutral hydrogen atoms can absorb/scatter ultraviolet photons, and which lead to the Gunn-Peterson effect, dark gap and dark pixel analyses, quasar near zones and damping wing absorption. Finally, the future prospects for using quasars as probes of reionization are described.

1 Introduction

Cosmological hydrogen reionization was largely complete by about a billion years after the Big Bang, when the Universe was just $\sim 7\%$ of its current age (~ 13.8 Gyr). To learn directly about the process of reionization requires that signals – most obviously photons – are detected from this epoch or earlier (although inferences can also be made from sources seen at later times). The cosmic microwave background (CMB) radiation can be used as a “back-light” to probe reionization, providing important integral constraints on the density of free electrons (Chapter X) and 21 cm radiation from neutral hydrogen (HI) present in the early Universe should be able to provide a wealth of information in the future (Chapter X), but the most direct probes are the luminous astronomical objects that had formed before reionization was complete.

Seen with redshifts of $z \gtrsim 6$, these sources are amongst the most distant currently known to astronomy. Ordinary galaxies at these distances are too faint to provide

Astrophysics Group, Blackett Laboratory, Imperial College London, London SW7 2AZ, UK
e-mail: mortlock@ic.ac.uk

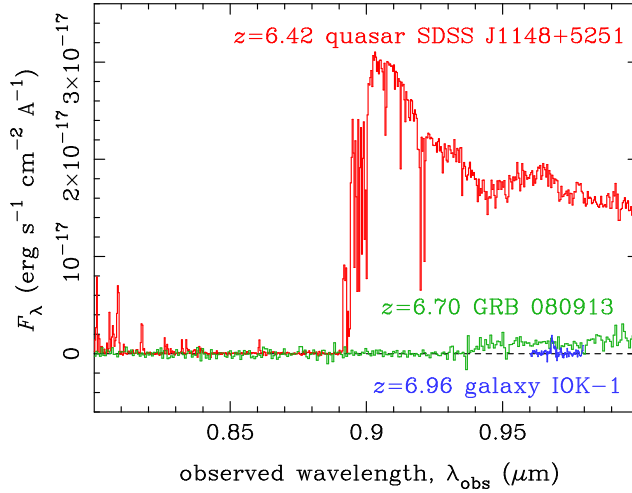


Fig. 1 Spectra of representative high redshift sources: the $z = 6.42$ quasar SDSS J1148+5251 [7, 8]; GRB 080913 at $z = 6.70$ [9]; and the Ly α -emitting $z = 6.96$ galaxy IOK-1 [10].

much information individually, but their properties as a population are sufficiently well constrained for them to be confirmed as the dominant source of ionizing photons (Chapter X). Much brighter gamma-ray bursts (GRBs) have also been detected during the reionization epoch; their largely featureless spectra are ideal for absorption studies, although a combination of their rarity and transience have so far limited their effectiveness as reionization probes (Chapter X). The other main class of astronomical object known to have existed at these early times are quasars. They have high luminosities (comparable to GRBs at peak and thousands of times brighter than field galaxies, as illustrated in Fig. 1) but are extremely rare, with only a few per thousand deg^2 on the sky.

The use of quasars as probes of reionization is explored here, updating previous reviews ([1, 2] and the introductions to, e.g., [3, 4]) and unifying some of the varied theoretical approaches taken in cosmology textbooks (e.g., [5, 6]). The emphasis is mostly on the underlying theory and methods, as these are most likely to remain robust to future discoveries, although the more secure results are given as well. The context is given by the cosmological model (Section 2) and a summary of the results of quasar searches (Section 3). The absorption properties of neutral hydrogen (Section 4) lead to a number of distinct constraints on the neutral fraction of hydrogen in the high-redshift Universe (Sections 5, 6 and 7). With new data and better models – and ways of comparing the two – these constraints will steadily be improved in the future (Section 8).

2 Cosmology

Cosmological distances, volumes, etc., are calculated assuming that the Universe is spatially flat, the normalised matter density is $\Omega_m = 0.3$, the normalised cosmological constant is $\Omega_\Lambda = 1 - \Omega_m = 0.7$, the normalised baryon density is $\Omega_b = 0.04$, the primordial helium fraction (by mass) is $Y = 0.24$, and the Hubble constant is $H_0 = 70 \text{ km s}^{-1} \text{ Mpc}^{-1}$.

All lengths, volumes, etc., are proper, *not* co-moving, with the exception of the mean total density of hydrogen (i.e., both neutral and ionized), which is given in terms of the current (and hence co-moving) value,

$$\bar{n}_{\text{H},0} = \frac{3H_0^2(1-Y)\Omega_b}{8\pi G m_p} \simeq 0.17 \text{ atoms m}^{-3}, \quad (1)$$

where $G = 6.67 \times 10^{-11} \text{ m}^3 \text{ kg}^{-1} \text{ s}^{-2}$ is Newton's gravitational constant and $m_p = 1.67 \times 10^{-27} \text{ kg}$ is the proton mass. The mean proper density of neutral hydrogen in the inter-galactic medium (IGM) at redshift z can hence be written in terms of the evolving mean neutral fraction, $x_{\text{HI}}(z)$, as

$$\bar{n}_{\text{HI}}(z) = \bar{n}_{\text{H},0}(1+z)^3 x_{\text{HI}}(z) = \frac{3H_0^2(1-Y)\Omega_b(1+z)^3 x_{\text{HI}}(z)}{8\pi G m_p}. \quad (2)$$

Deviations from uniformity that arise in particular from the inhomogeneous or ‘‘patchy’’ nature of reionization (Chapter X) are discussed where relevant.

The Hubble parameter evolves with redshift according to

$$H(z) = H_0 [\Omega_m(1+z)^3 + \Omega_\Lambda - (\Omega_m + \Omega_\Lambda - 1)(1+z)]^{1/2} \simeq H_0 \Omega_m^{1/2} (1+z)^{3/2}, \quad (3)$$

where the second expression is accurate to per cent level for the redshifts of $z \gtrsim 5$ that are relevant here. In this regime a redshift of z corresponds to a time (measured since the Big Bang at time $t = 0$) of

$$t \simeq \frac{2}{3\Omega_m^{1/2} H_0 (1+z)^{3/2}} \simeq 0.92 \left(\frac{1+z}{7} \right)^{-3/2} \text{ Gyr}. \quad (4)$$

The change in redshift, dz , that occurs while a photon moves a (proper) distance dl towards Earth is given implicitly by

$$dl = c dt = \frac{-c}{(1+z)H(z)} dz \simeq \frac{-c}{H_0 \Omega_m^{1/2} (1+z)^{5/2}} dz, \quad (5)$$

where the last expression is, again, accurate for $z \gtrsim 5$. This relationship is needed both for optical depth calculations (Section 4.2) and to convert from small wavelength shifts to local physical scales (Section 6). In particular, a photon emitted by a distant source at redshift $z_{\text{src}} \gtrsim 5$ would reach a small (proper) distance R at a

cosmological time corresponding to a redshift of

$$z \simeq z_{\text{src}} - \frac{R}{c/H_0} \Omega_m^{1/2} (1 + z_{\text{src}})^{5/2}, \quad (6)$$

where it is assumed that the light travel time, R/c , is much smaller than the Hubble time, $1/H(z_{\text{src}})$, at that redshift. If the photon's wavelength had been λ when it was at distance R from the source then it would now be observed with a wavelength of

$$\lambda_{\text{obs}} \simeq \lambda (1 + z_{\text{src}}) \left[1 - \frac{R}{c/H_0} \Omega_m^{1/2} (1 + z_{\text{src}})^{3/2} \right]. \quad (7)$$

3 High-redshift quasars

Quasars were first identified in 1963 [11, 12] as bright point-sources with what were then thought of as unusually high redshifts. The nature of these objects was unknown at that time, although a consensus has since been reached that a quasar is the observable manifestation of the hot, compressed gas in an accretion disk around a super-massive black hole in the centre of an otherwise ordinary galaxy (e.g., [13]).

The physical nature of quasars is, however, largely irrelevant to their utility as probes of reionization; more important is that bright quasars (with bolometric luminosities of $L \gtrsim 10^{40} \text{ W} \simeq 10^{13} L_{\odot}$) had already formed by the time the hydrogen in the IGM was undergoing reionization. These high-redshift quasars (HZQs) are seen as unresolved point-sources with optical or near-infrared (NIR) flux densities of $\sim 0.01 \text{ mJy}$, corresponding to (AB) magnitudes of ~ 20 , although there is (as discussed further in Section 5) almost complete absorption blueward of the Ly α break (Section 4.1) at an observed wavelength of $\lambda_{\text{obs}} \simeq [0.85 + 0.12(z - 6)] \mu\text{m}$. Critically, high quality spectra of $z \gtrsim 6$ quasars can be obtained with the current generation of large (i.e., 8 m class) ground-based telescopes. Such observations make detailed absorption studies possible, and most of the reionization constraints discussed below are based on measurements of this sort.

The practical utility of quasars as probes of reionization is limited primarily by the fact that they are so rare, with a number density of just a few per cubic Gpc at $z \simeq 6$ [14, 15], corresponding to a few per thousand deg^2 on the sky. Fortunately, there are a number of compelling reasons (including finding more HZQs!) to undertake wide-field sky surveys (Section 3.1), with the result that the number of known HZQs is now close to one hundred (Section 3.2).

3.1 High-redshift quasar surveys

Observational astronomy is increasingly based on large (i.e., either wide and/or deep) sky surveys, particularly at the optical and NIR wavelengths that can be used

to identify $z \gtrsim 6$ sources from their Ly α break. (It is also possible to identify HZQs by exploiting the fact that some are radio-loud [16, 17, 18], but the optical-NIR search methods have resulted in the vast majority of discoveries to date.) The Sloan Digital Sky Survey (SDSS [19]), the Canada France Hawaii Telescope Legacy Survey (CFHTLS [20, 21]), the Panoramic Survey Telescope And Rapid Response System (Pan-STARRS [22, 23]), the UKIRT Infrared Deep Sky Survey (UKIDSS [24]) and the Visible and Infrared Survey Telescope for Astronomy (VISTA [25]) have, between them, observed over half the sky and catalogued more than a billion sources in the optical and NIR. All these surveys have the combination of area, depth and wavelength coverage needed to detect significant numbers of HZQs, although it is only the surveys with multi-band NIR coverage (UKIDSS, VISTA and, to a lesser degree, Pan-STARRS) that can probe $z \gtrsim 6.5$.

All the above surveys have discovered several HZQs (including a number of rediscoveries of previously known objects, an important cross-check). While the search process is complicated (see, e.g., [14, 26, 27, 28]), there do not appear to be any significant selection effects that would bias the inferences about reionization made from the sub-set of quasars that have been found. In particular, even though the majority of the quasars listed in Table 1 were initially discovered by exploiting the fact that they have no appreciable flux in all but the reddest optical passbands, there is no suggestion of a sub-population of $z \gtrsim 6$ sources without sharp Ly α breaks that have been missed. The corollary is that any HZQ can be used to provide constraints on the evolution of x_{HI} , although the fact that reionization is expected to be a patchy process (Chapter X) means that that multiple lines-of-sight are needed to extrapolate to the global reionization history.

3.2 Currently known high-redshift quasars

The above surveys – and, to a lesser degree, other searches – have, as of mid-2015, resulted in the discovery of 89 quasars with redshifts of $z \geq 5.8$. These are listed in Table 1¹ and illustrated in Fig. 2.

For reionization studies it is the most distant and the most luminous² which are most important. The HZQs which have been subject to the most scrutiny so far are:

- SDSS J1030+0524 [14] at $z = 6.30$, which was the most distant known quasar when it was discovered and is currently the third brightest with $z \geq 6$;
- SDSS J1048+4637 [7] at $z = 6.26$, which is currently the second brightest known quasar with $z \geq 6$;
- SDSS J1148+5251 [7] at $z = 6.42$, which was also the most distant known quasar when it was discovered and is currently the brightest known with $z \geq 6$;

¹ An up-to-date and expanded version of this table in machine-readable form is available from the author.

² Strictly, it is the flux at Earth which is the relevant quantity but, as can be seen from Fig. 2, the decrease in flux with redshift across the reionization epoch is considerably smaller than the range of quasar luminosities, so M_{1450} is an excellent proxy for the likely utility of any single source.

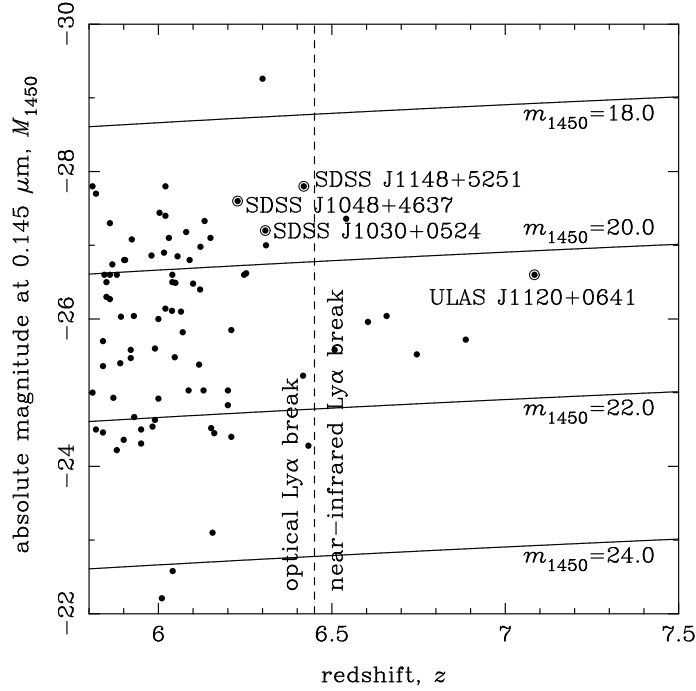


Fig. 2 Redshifts and absolute magnitudes (measured at a rest-frame wavelength of $\lambda_{\text{em}} = 0.145$ micron) of the known $z \geq 5.8$ quasars listed in Table 1. The four quasars discussed in Section 3.2 are labelled explicitly. The solid curves trace lines of constant AB magnitude, m_{1450} , i.e., the flux density at an observed wavelength of $\lambda_{\text{obs}} = 0.145(1+z)$ μm . The dashed vertical line indicates the redshift above which, due to Ly α absorption by the IGM, sources are detectable only at NIR wavelengths.

- ULAS J1120+0641 [29] at $z = 7.08$, which is currently the most distant quasar known.

These four³ objects are highlighted in Fig. 2, indicating why SDSS J1148+5251 and ULAS J1120+0641 in particular are central to a number of the reionization constraints discussed below.

Table 1 Known high-redshift ($z \geq 5.8$) quasars

ID	z	M_{1450}	z_{NZ}	reference(s)
SDSS J000239.39+255034.8	5.820 ± 0.020	-27.70 ± 0.00	5.65 ± 0.01	[32, 33]

Continued on next page

³ The recently discovered quasars PSO J0226+0302 [30], at $z = 6.53$ and unusually bright, and SDSS J0100+2802 [31], at $z = 6.30$ and a factor of a few more luminous than any other known HZQ, will presumably be key sources in the future, but as yet have not been subject to full follow-up campaigns.

Table 1 Continued from previous page

ID	z	M_{1450}	z_{NZ}	reference(s)
SDSS J000552.34-000655.8	5.850 ± 0.003	-26.50 ± 0.10	5.77 ± 0.01	[32, 34, 33]
SDSS J000825.77-062604.6	5.929 ± 0.003	-26.04 ± 0.09	...	[35]
PSO J002806.56+045725.7	6.040 ± 0.030	-26.50 ± 0.10	...	[36, 35]
CFHQS J003311.40-012524.9	6.130 ± 0.020	-25.03 ± 0.10	...	[26]
CFHQS J005006.67+344522.6	6.253 ± 0.003	-26.62 ± 0.10	...	[37, 38]
CFHQS J005502.91+014618.3	5.983 ± 0.004	-24.54 ± 0.10	...	[39, 37]
SDSS J010013.02+280225.8	6.300 ± 0.010	-29.26 ± 0.20	...	[31]
CFHQS J010250.64-021809.9	5.950 ± 0.020	-24.31 ± 0.10	...	[39]
VHS J010953.13-304726.3	6.745 ± 0.010	-25.52 ± 0.15	...	[40]
CFHQS J013603.17+022605.7	6.210 ± 0.020	-24.40 ± 0.10	...	[37]
ATLAS J014243.70-332745.7	6.020 ± 0.030	-27.80 ± 0.20	...	[41]
ULAS J014837.64+060020.0	5.923 ± 0.003	-27.08 ± 0.06	...	[42, 36, 43, 35]
ATLAS J015957.96-363356.9	6.310 ± 0.030	-27.00 ± 0.10	...	[41]
CFHQS J021013.19-045620.9	6.432 ± 0.001	-24.28 ± 0.10	6.41 ± 0.02	[38, 44]
CFHQS J021627.81-045534.1	6.010 ± 0.020	-22.21 ± 0.10	...	[39]
CFHQS J022122.71-080251.5	6.161 ± 0.014	-24.45 ± 0.10	...	[37, 38]
PSO J022601.88+030259.4	6.541 ± 0.002	-27.36 ± 0.03	6.46 ± 0.01	[30, 36]
CFHQS J022743.29-060530.2	6.200 ± 0.020	-25.03 ± 0.10	...	[39]
PSO J023152.96-285020.1	5.990 ± 0.020	-25.60 ± 0.10	...	[36]
SDSS J023930.24-004505.4	5.820 ± 0.030	-24.50 ± 0.12	...	[45]
SDSS J030331.40-001912.9	6.070 ± 0.001	-25.82 ± 0.10	6.00 ± 0.01	[27, 33]
VHS J030516.92-315056.0	6.604 ± 0.008	-25.96 ± 0.06	...	[40]
CFHQS J031649.87-134032.3	5.990 ± 0.020	-24.63 ± 0.10	...	[37]
VIKINGKIDS J0328-3252	5.850 ± 0.030	[46, 41]
VISTA J032835.51-325322.9	5.860 ± 0.030	-26.60 ± 0.04	...	[46]
SDSS J035349.72+010404.4	6.049 ± 0.004	-26.49 ± 0.08	6.02 ± 0.01	[27, 33]
DES J045401.79-444831.1	6.100 ± 0.030	-26.48 ± 0.10	...	[47]
SDSS J081827.40+172251.8	6.020 ± 0.020	-27.40 ± 0.10	5.89 ± 0.02	[48, 33]
ULAS J082813.42+263355.6	6.100 ± 0.020	[42]
SDSS J083643.86+005453.2	5.810 ± 0.007	-27.80 ± 0.10	5.62 ± 0.01	[14, 33]
VISTA J083955.3+001554.2	5.840 ± 0.040	-25.36 ± 0.11	...	[46]
SDSS J084035.09+562419.9	5.844 ± 0.002	-26.60 ± 0.10	5.69 ± 0.01	[48, 33]
SDSS J084119.52+290504.4	5.980 ± 0.020	-26.86 ± 0.10	5.81 ± 0.01	[49, 33]
SDSS J084229.23+121848.2	6.080 ± 0.020	-27.18 ± 0.03	...	[50, 51]
SDSS J084229.43+121850.5	6.055 ± 0.003	-26.85 ± 0.09	...	[35]
SDSS J085048.25+324647.9	5.867 ± 0.007	-26.74 ± 0.08	...	[35]
SDSS J103027.10+052455.0	6.308 ± 0.007	-27.20 ± 0.10	6.21 ± 0.01	[14, 33]
SDSS J104845.05+463718.3	6.228 ± 0.002	-27.60 ± 0.10	6.16 ± 0.01	[7, 33]
CFHQS J104928.61-090620.4	5.920 ± 0.020	-25.58 ± 0.10	...	[37]
PSO J111033.98-132945.6	6.508 ± 0.001	-25.58 ± 0.13	6.48 ± 0.01	[30]
ULAS J112001.48+064124.3	7.084 ± 0.000	-26.60 ± 0.10	7.04 ± 0.01	[29, 52]
SDSS J113717.70+354957.0	6.030 ± 0.020	-27.10 ± 0.10	5.91 ± 0.01	[48, 33]
ULAS J114803.29+070208.3	6.200 ± 0.020	[42, 36]
SDSS J114816.64+525150.3	6.419 ± 0.002	-27.80 ± 0.10	6.33 ± 0.01	[7, 33]
VISTA J114833.18+005642.2	5.840 ± 0.030	-24.46 ± 0.11	...	[46]
ULAS J120737.44+063010.4	6.040 ± 0.003	-26.60 ± 0.11	...	[42, 36, 35]
PSO J121311.81-124603.5	5.860 ± 0.020	-27.30 ± 0.10	...	[36]
VISTA J121516.87+002324.7	5.930 ± 0.030	-24.67 ± 0.14	...	[46]
PSO J122913.21+041927.7	5.890 ± 0.020	-25.40 ± 0.10	...	[36]
ULAS J124340.81+252923.9	5.830 ± 0.020	[42, 36]
SDSS J125051.90+313022.0	6.150 ± 0.020	-27.10 ± 0.10	6.03 ± 0.01	[48, 33]

Continued on next page

Table 1 Continued from previous page

ID	z	M_{1450}	z_{NZ}	reference(s)
SDSS J125757.47+634937.2	6.020 ± 0.030	-26.14 ± 0.12	...	[35]
SDSS J130608.26+035626.3	6.016 ± 0.007	-26.90 ± 0.10	5.92 ± 0.01	[14, 33]
ULAS J131911.29+095051.4	6.133 ± 0.001	-27.33 ± 0.10	6.04 ± 0.01	[53, 54, 36]
SDSS J133550.81+353315.8	5.901 ± 0.002	-26.80 ± 0.10	5.89 ± 0.01	[48, 33]
SDSS J140319.13+090250.9	5.860 ± 0.030	-26.27 ± 0.11	...	[35]
PSO J140329.33-120034.1	5.840 ± 0.020	-25.70 ± 0.10	...	[36]
SDSS J141111.28+121737.3	5.904 ± 0.007	-26.80 ± 0.10	5.82 ± 0.01	[32, 33]
PSO J141327.12-223342.3	5.880 ± 0.020	-26.60 ± 0.10	...	[36]
NDWFS J142516.30+325409.0	5.892 ± 0.002	-26.03 ± 0.10	5.76 ± 0.01	[17, 33]
FIRST J142738.59+331242.0	6.120 ± 0.020	-26.40 ± 0.10	...	[16]
CFHQS J142952.17+544717.7	6.210 ± 0.020	-25.85 ± 0.10	...	[37]
SDSS J143611.70+500707.0	5.850 ± 0.020	-26.30 ± 0.10	5.72 ± 0.01	[48, 33]
CFHQS J150941.78-174926.8	6.121 ± 0.003	-26.98 ± 0.10	...	[26, 38]
SDSS J160254.18+422822.9	6.090 ± 0.020	-26.80 ± 0.10	5.94 ± 0.01	[32, 33]
ELIAS J160349.07+551032.3	6.041 ± 0.020	-22.58 ± 0.13	...	[55]
ULAS J160937.28+304147.7	6.080 ± 0.020	[42]
SDSS J162331.81+311200.5	6.247 ± 0.007	-26.60 ± 0.10	6.16 ± 0.01	[32, 33]
SDSS J163033.90+401209.6	6.065 ± 0.007	-26.10 ± 0.10	5.94 ± 0.01	[7, 33]
CFHQS J164121.64+375520.5	6.047 ± 0.003	-25.48 ± 0.10	...	[26, 37]
SDSS J205321.77+004706.8	5.920 ± 0.030	-25.47 ± 0.07	...	[45]
SDSS J205406.49-000514.8	6.039 ± 0.000	-26.11 ± 0.09	5.97 ± 0.01	[27, 33, 54]
CFHQS J210054.62-171522.5	6.087 ± 0.003	-25.03 ± 0.10	...	[37, 38]
SDSS J214755.41+010755.3	5.810 ± 0.030	-25.00 ± 0.10	...	[45]
VIMOS J221917.22+010248.9	6.156 ± 0.020	-23.10 ± 0.11	...	[55]
SDSS J222843.54+011032.2	5.950 ± 0.020	-24.50 ± 0.10	...	[18]
CFHQS J222901.65+145709.0	6.152 ± 0.003	-24.52 ± 0.10	...	[37, 38]
PSO J223255.15-293032.2	6.658 ± 0.007	-26.04 ± 0.09	6.55 ± 0.01	[30]
PSO J224048.98-183943.8	6.000 ± 0.020	-26.00 ± 0.10	...	[36, 36]
CFHQS J224237.55+033421.6	5.880 ± 0.020	-24.22 ± 0.10	...	[37]
SDSS J230735.35+003149.4	5.870 ± 0.030	-24.93 ± 0.10	...	[45]
SDSS J231038.89+185519.9	6.003 ± 0.000	-27.44 ± 0.10	...	[50, 54, 36]
SDSS J231546.57-002358.1	6.117 ± 0.006	-25.38 ± 0.08	6.05 ± 0.01	[27, 33]
CFHQS J231802.80-024634.0	6.200 ± 0.020	-24.83 ± 0.10	...	[39]
CFHQS J232908.28-030158.8	6.417 ± 0.002	-25.23 ± 0.10	6.35 ± 0.01	[26, 37, 33]
CFHQS J232914.46-040324.1	5.900 ± 0.020	-24.36 ± 0.10	...	[39]
VHS J234833.34-305410.0	6.886 ± 0.009	-25.72 ± 0.14	...	[40]
SDSS J235651.58+002333.3	6.000 ± 0.030	-24.92 ± 0.10	...	[45]

4 Line-of-sight absorption by neutral hydrogen

The most direct way in which quasars reveal the (re-)ionization history of the Universe is as sources of photons from which the absorption due to any intervening neutral hydrogen can be inferred. Critically, quasars have sufficiently similar spectra – broad emission lines superimposed on a blue continuum – that the fraction of flux transmitted can be estimated reliably. It is also important that the cosmological density of hydrogen is sufficient to produce appreciable absorption even if the

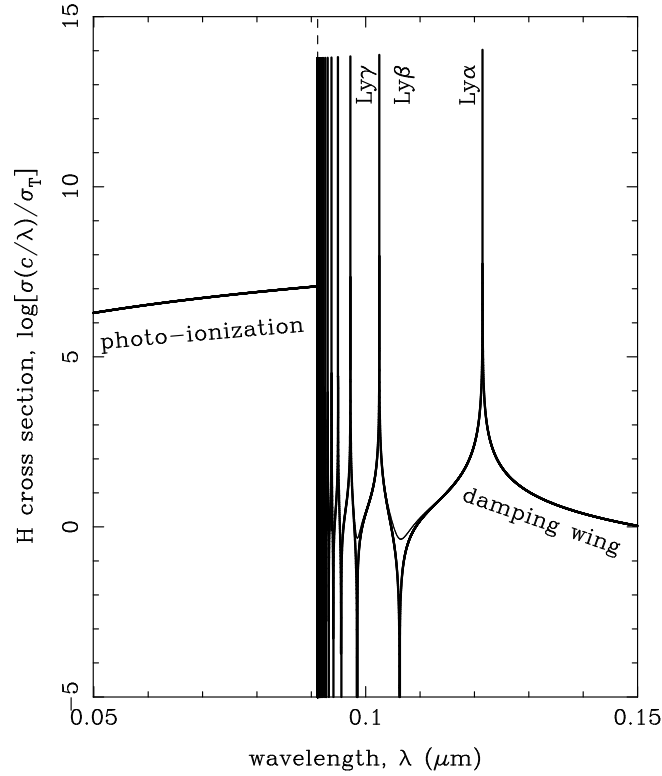


Fig. 3 Neutral hydrogen absorption cross section as a function of photon wavelength, λ . The Rayleigh scattering contribution (Eq. 11, thick curve) dominates, although the additional contributions from Raman scattering can be seen between the Ly α , Ly β and Ly γ resonances (thin curve). (Despite appearances, the integrated cross section in a thin band of width $\Delta\lambda$ in the Lyman limit region near the ionization threshold of $\lambda = 0.091 \mu\text{m}$ is comparable to the smooth photo-ionization cross section.)

neutral fraction is low; conversely, there are some wavelengths at which only partial absorption is produced even by a completely neutral IGM.

4.1 Scattering of photons by a neutral hydrogen atom

A neutral hydrogen atom with its electron in the ground ($1s$) state can absorb (and often re-emit, i.e., effectively scatter) an incident photon via a number of distinct quantum mechanical channels. The resultant cross section has the form

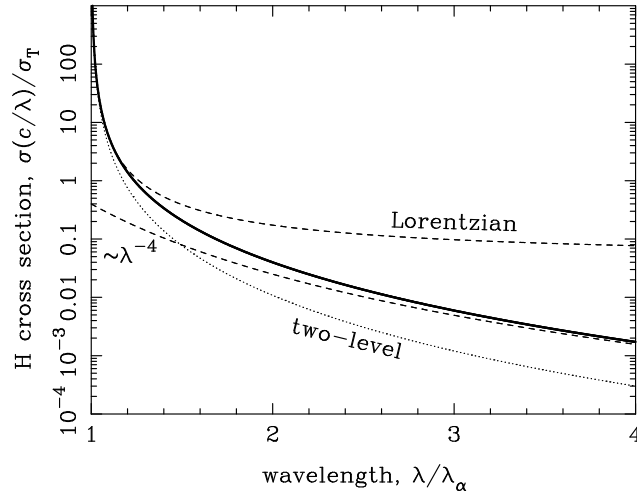


Fig. 4 Ly α damping wing cross section, shown as a function of photon wavelength, λ . The full cross section (Eq. 11, solid curve) is compared to the Lorentzian approximation (Eq. 14, dashed curve) and the low-frequency limiting form (Eq. 16, dashed curve) and the two-level model (Eq. 18, dotted curve) commonly used in calculations of the IGM damping wing.

$$\sigma(\nu) = \sigma_{\text{Rayleigh}}(\nu) + \sigma_{\text{Raman}}(\nu) + \sigma_{\text{phot-ion}}(\nu) + \dots, \quad (8)$$

where ν is the frequency⁴ of the incident photon and the terms correspond to elastic Rayleigh scattering (in which the electron returns to the ground state) inelastic Raman scattering (in which the electron is left in an intermediate excited state), photo-ionization (in which the electron is removed from the atom), etc. The relative contributions of these processes are illustrated in Fig. 3. A first principles calculation (e.g., [56, 57, 58]) requires evaluation of the overlap integrals of the wave functions corresponding to the initial, intermediate (i.e., excited) and final states, but the essential phenomenology relevant to reionization studies can be understood without recourse to the full formalism.

Most important here is the Rayleigh scattering process, which includes all the Lyman series transitions, in particular the strong Ly α resonance (in which a hydrogen atom's electron is excited from the $1s$ ground state to the $2p$ energy level and then returns to the ground state) and the slightly weaker Ly β ($1s \rightarrow 3p$), and Ly γ ($1s \rightarrow 4p$) transitions. These higher order transitions are also Raman scatter-

⁴ It would be more in keeping with astronomical conventions to give the cross section in terms of wavelength, $\lambda = c/\nu$; and it is standard in quantum physics to use angular frequency, $\omega = 2\pi\nu$, or sometimes energy, $E = h\nu$. Frequency is used here it is more directly linked to the physics of the scattering processes than wavelength, while being more commonly used in astronomy than angular frequency. The argument of the cross section $\sigma(\cdot)$ is *always* frequency here.

Table 2 Properties of the Lyman series transitions

name	n transition	wavelength, $\lambda_{1,n}$	decay rate, $\Lambda_{1,n}$	oscillator strength, $f_{1,n}$
Ly α	$2\ 2p \rightarrow 1s$	$0.12157\ \mu\text{m}$	$6.265 \times 10^8\ \text{s}^{-1}$	0.4162
Ly β	$3\ 3p \rightarrow 1s$	$0.10257\ \mu\text{m}$	$1.672 \times 10^8\ \text{s}^{-1}$	0.0791
Ly γ	$4\ 4p \rightarrow 1s$	$0.97254\ \mu\text{m}$	$0.682 \times 10^8\ \text{s}^{-1}$	0.0290
Ly δ	$5\ 5p \rightarrow 1s$	$0.94974\ \mu\text{m}$	$0.344 \times 10^8\ \text{s}^{-1}$	0.0139
...				
	$\gg 1\ np \rightarrow 1s$	$\frac{0.91175}{1-1/n^2}\ \mu\text{m}$	$\frac{41.80 \times 10^8}{n^3}\ \text{s}^{-1}$	$\frac{1.563}{n^3}$
...				
Ly limit	∞	$0.91175\ \mu\text{m}$		

ing resonances, but the relative contribution from these channels is only significant away from the resonances, as can be seen from Fig. 3. The n th electron energy level is $E_n = E_\infty(1 - 1/n^2)$, where $E_\infty = m_e e^4 / (8\epsilon_0^2 h^2) \simeq 13.6\ \text{eV}$ is the Rydberg energy, $m_e = 9.109 \times 10^{-31}\ \text{kg}$ is the electron mass, $e = 1.602 \times 10^{-19}\ \text{C}$ is the electron charge, $\epsilon_0 = 8.854 \times 10^{-12}\ \text{F m}^{-1}$ is the permittivity of free space⁵, and $h = 6.626 \times 10^{-34}\ \text{m}^2\ \text{kg}\ \text{s}^{-1}$ is Planck's constant. The fiducial wavelength and frequency of a photon associated with the $1s \rightarrow np$ transition are hence $\lambda_{1,n} = hc/[E_\infty(1 - 1/n^2)]$ and $\nu_{1,n} = [E_\infty(1 - 1/n^2)]/h$, respectively. The spontaneous decay rate (i.e., the Einstein A coefficient) of the transition is

$$\Lambda_{1,n} = \frac{\pi e^{10} f_{1,n} m_e}{96 c^3 \epsilon_0^5 h^6} \left(1 - \frac{1}{n^2}\right)^2, \quad (9)$$

with associated oscillator strength

$$f_{1,n} = \frac{256 n^5 (n-1)^{2n-4}}{3(n+1)^{2n+4}}. \quad (10)$$

These quantities are tabulated for the first few Lyman series transitions in Table 2.

The full Rayleigh scattering cross section is obtained by squaring the sum over the complex amplitudes associated with the various excited states (as interference is possible), the result of which can be approximated as (cf. [59, 60, 61])

$$\sigma(\nu) = \sigma_T \left| \sum_{n=2}^{\infty} f_{1,n} \frac{\nu^2}{\nu_{1,n}^2 - \nu^2 + i\Lambda_{1,n}\nu_{1,n}/(2\pi)} + \int_{E_\infty}^{\infty} \frac{df}{dE} \frac{1}{E^2/(h\nu)^2 - 1} dE \right|^2, \quad (11)$$

where $\sigma_T = 8\pi/3[e^2/(4\pi\epsilon_0 m_e c^2)]^2 \simeq 6.65 \times 10^{-29}\ \text{m}^2$ is the Thomson cross section, and the spectrum of oscillator strengths for the unbound states is [60, 62]

$$\frac{df}{dE} = \Theta(E - E_\infty) \frac{128 \exp\{-4 \arctan[(E/E_\infty - 1)^{1/2}]/(E/E_\infty - 1)^{1/2}\}}{3E_\infty(E/E_\infty)^4 \{1 - \exp[-2\pi/(E/E_\infty - 1)^{1/2}]\}}, \quad (12)$$

⁵ SI units are used here; in cgs units $\epsilon_0 = 1/(4\pi)$ is effectively dimensionless.

with $\Theta(\cdot)$ the Heaviside step function. The first term in Eq. 11 corresponds to the bound excited states of the Lyman series. This sum is dominated by the low- n terms and can be truncated in practice, or evaluated using a Taylor series expansion [60] or a fitting formula [61, 63].

The main features of the Rayleigh scattering cross section, shown in Fig. 3, are the resonant Lyman series peaks and the long-wavelength damping wing. While these both come from the same underlying physics, their observational manifestations are sufficiently distinct that it is useful to consider them separately.

4.1.1 Resonant absorption

Near any of the Lyman series resonances the cross section given in Eq. 11 is dominated by a single term in the sum. For the $1s \rightarrow np$ resonance this leads to

$$\sigma_{\text{Lor},n}(v) \simeq \sigma_{\text{T}} f_{1,n}^2 \frac{v^4}{(v^2 - v_{1,n}^2)^2 + \Lambda_{1,n}^2 v_{1,n}^2 / (4\pi^2)} \quad (13)$$

$$\simeq \sigma_{\text{T}} \frac{f_{1,n}^2}{4} \frac{v_{1,n}^2}{(v - v_{1,n})^2 + \Lambda_{1,n}^2 / (16\pi^2)} \quad \text{if } |v - v_{1,n}| \ll v_{1,n}, \quad (14)$$

the Lorentzian form that is often used to analyse discrete H I concentrations (such as in the Ly α “forest” and the high column density systems considered in Section 7). These resonances are extremely sharp – for the Ly α transition $\Lambda_{\alpha}/v_{\alpha} \simeq 10^{-7}$, so the peak at a wavelength of $\lambda_{\alpha} \simeq 0.12 \mu\text{m}$ has an characteristic width of just $\sim 10^{-8} \mu\text{m}$ – and are completely unresolved in Fig. 3. The cross section at resonance is correspondingly high, being given almost exactly by $\sigma(v_{1,n}) = 4\pi^2 \sigma_{\text{T}} f_{1,n}^2 v_{1,n}^2 / \Lambda_{1,n}^2$. In the case of Ly α this is $\sigma_{\alpha} \simeq 4.41 \times 10^{-16} \text{ m}^2$.

While there is no physical reason that the integral of $\sigma(v)$ over wavelength should be finite – indeed, the full form of Eq. 11 cannot be normalised to give a probability distribution in v – adopting Eq. 14 implies that $\int_0^{\infty} dv \sigma_{\text{Lor},n}(v) \simeq \int_{-\infty}^{\infty} dv \sigma_{\text{Lor},n}(v) = \pi^2 \sigma_{\text{T}} f_{1,n}^2 v_{1,n}^2 / \Lambda_{1,n}$. Treating the absorption at each resonance as completely mono-chromatic then leads to the useful approximation that the full cross section is

$$\sigma(v) \simeq \sigma_{\text{T}} \sum_{n=2}^{\infty} \frac{\pi^2 f_{1,n}^2 v_{1,n}^2}{\Lambda_{1,n}} \delta_{\text{D}}(v - v_{1,n}), \quad (15)$$

where $\delta_{\text{D}}(\cdot)$ is the Dirac delta function. This is used in the standard derivation of the IGM optical depth given in Section 5.

4.1.2 Damped absorption

Redward of the Ly α resonance, the damped absorption wing includes contributions from all the excited states. The full damping wing cross section (i.e., extending to the Ly α resonance) can be evaluated numerically from the formula given in Eq. 11,

although transmission is typically close to zero just redward of the Ly α line so there is little practical need to match the in-resonance form of $\sigma(\nu)$ precisely in calculations of the damping wing absorption (Section 7). This opens up the possibility of using one of several available approximations [60, 61, 63].

In the low frequency limit the ν -dependence of all the terms in Eq. 11 is such that the classical $\sigma(\nu) \propto \nu^4$ Rayleigh scattering result holds for each individually; they sum to give [60, 61]

$$\sigma(\nu) \simeq 0.399 \sigma_{\text{T}} \left(\frac{\nu}{\nu_{\alpha}} \right)^4 \quad \text{if } \nu \ll \nu_{\alpha}, \quad (16)$$

where $\nu_{\alpha} = \nu_{1,2}$ is the frequency of the Ly α resonance.

That said, extrapolation of the $n = 2$ Lorentzian profile of Eq. 14 to lower frequencies, which gives

$$\sigma_{\text{Lor},2}(\nu) \simeq \sigma_{\text{T}} f_{1,2}^2 \frac{1}{4(\nu/\nu_{\alpha} - 1)^2} \quad \text{if } \nu - \nu_{\alpha} \ll \Lambda_{1,2}, \quad (17)$$

does not yield a good approximation to the damping wing, as can be seen from Fig. 4. This point was made by Miralda-Escudé [64], who instead advocated using the form of $\sigma(\nu)$ derived by Peebles [5] and based in turn on a classic quantum mechanics calculation [65]. The underlying model is that a hydrogen atom is a two-level system in which a bound electron is restricted to the $1s$ or $2p$ states, which yields a cross section of [5, 64, 65]

$$\sigma_{2\text{L}}(\nu) = \sigma_{\text{T}} \frac{f_{1,2}^2}{4} \frac{\nu_{\alpha}^2 (\nu/\nu_{\alpha})^4}{(\nu - \nu_{\alpha})^2 + \Lambda_{1,2}^2 / (16\pi^2) (\nu/\nu_{\alpha})^6} \quad \text{if } \nu \gtrsim \nu_{\alpha} \quad (18)$$

$$\simeq \sigma_{\text{T}} f_{1,2}^2 \frac{(\nu/\nu_{\alpha})^4}{4(\nu/\nu_{\alpha} - 1)^2} \quad \text{if } \nu - \nu_{\alpha} \ll \Lambda_{1,2}. \quad (19)$$

The first formula includes the Ly α resonance, correctly matching Eq. 14 if $\nu \simeq \nu_{\alpha}$; and the $(\nu/\nu_{\alpha})^4$ term in the numerator of both expressions gives a full damping wing. In the low frequency limit, however,

$$\sigma_{2\text{L}}(\nu) \simeq 0.0433 \sigma_{\text{T}} \left(\frac{\nu}{\nu_{\alpha}} \right)^4 \quad \text{if } \nu \ll \nu_{\alpha}, \quad (20)$$

which is a factor of ~ 10 smaller than the correct limit given in Eq. 16. The reason [5, 61] for this discrepancy is the omission of the contributions from the other excited states ($3p$, $4p$, etc., as well as the unbound continuum), all of which contribute to Rayleigh scattering.

Rather ironically, the Lorentzian form given in Eq. 14 is, in practice, a more useful approximation to the red damping wing of the Ly α line. Even though the implied low frequency cross section has the wrong limiting form, with $\sigma_{\text{Lor},n}(\nu) \rightarrow 0.0433 \sigma_{\text{T}}$ as $\nu \rightarrow 0$, it is actually a good match for $0.9 \nu_{\alpha} \lesssim \nu \leq \nu_{\alpha}$ which dominates

the absorption. The implications of using different forms for $\sigma(v)$ to model the IGM damping wing are discussed in Section 7.

4.2 Absorption by neutral hydrogen in an expanding universe

The optical depth from the H I between observer and source is given by integrating the absorption cross section along the line-of-sight and also integrating over the (line-of-sight) velocity distribution at each point, although it is useful to consider the velocity integral as a separate convolution. A collection of H I atoms with (normalised) line-of-sight velocity distribution $\phi(v_{\parallel})$ can be treated as if *each* has the effective cross section

$$\sigma_{\text{eff}}(v) = \int_{-c}^c dv_{\parallel} \phi(v_{\parallel}) \sigma\left(\frac{v}{1+v_{\parallel}/c}\right) \simeq \int_{-\infty}^{\infty} dv_{\parallel} \phi(v_{\parallel}) \sigma[v(1-v_{\parallel}/c)] \quad (21)$$

where v_{\parallel} is defined to be positive away from the observer and it is assumed that the motions are non-relativistic.

If the motions are thermal then it is reasonable to adopt a Gaussian velocity distribution, $\phi(v_{\parallel}) = \exp[-v_{\parallel}^2/(2\sigma_{\parallel}^2)]/[(2\pi)^{1/2}\sigma_{\parallel}]$, where $\sigma_{\parallel} \ll c$ is the temperature-dependent (line-of-sight) velocity dispersion. The resultant form of $\sigma_{\text{eff}}(v)$ differs significantly from $\sigma(v)$ only near the sharp Lyman series resonances. The Lorentzian line profile of the $1s \rightarrow np$ transition given in Eq. 14 hence becomes

$$\sigma_{\text{eff},1,n}(v) = \sigma_{\text{T}} \frac{\pi^2 f_{1,n}^2 v_{1,n}^2}{\Lambda_{1,n}} \quad (22)$$

$$\times \int_{-\infty}^{\infty} dv' \frac{1}{(2\pi)^{1/2} v_{1,n} \sigma_{\parallel}/c} \exp\left[-\frac{1}{2} \left(\frac{v-v'}{v_{1,n} \sigma_{\parallel}/c}\right)^2\right] \frac{\Lambda_{1,n}/(4\pi)}{\pi[(v'-v_{1,n})^2 - \Lambda_{1,n}^2/(4\pi)^2]},$$

the Voigt profile form that is valid if $\sigma \ll c$ and $\Lambda_{1,n} \ll v_{1,n}$ (conditions which imply that the cross section is only significant for $v \simeq v_{1,n}$). The integral cannot be evaluated analytically, but a number of useful numerical approximation methods have been developed (e.g., [66, 67, 68, 69]). The second line of Eq. 22 is the convolution of a normal distribution and a Cauchy distribution, and so is itself a normalised Voigt distribution in v , centred at $v_{1,n}$. Far from resonance the Voigt profile has the same heavy tails as the Lorentzian, but close to resonance the peak is broadened to have Gaussian ‘‘core’’ of standard deviation $\sigma_v \simeq v_{1,n} \sigma_{\parallel}/c$. In the context of quasar reionization studies this is important for modelling the absorption by residual H I in quasar H II zones (Section 6) and also for correctly calculating the near-resonance form of the Ly α damping wing (Section 7).

For most of the results presented here, however, line-of-sight H I velocities can be ignored, either because the detailed shape of the resonant line profile itself is irrelevant (e.g., Section 5) or because it is only the long-wavelength limit of the

smooth damping wing that is important (most of Section 7). In this case the simplest approach is to assume that $\phi(v_{\parallel}) = \delta_{\text{D}}(v_{\parallel})$, in which case

$$\sigma_{\text{eff}}(v) = \sigma(v). \quad (23)$$

The infinitesimal optical depth to photons of wavelength λ along a (proper) line-of-sight interval of length $|dl|$ in a region with a local (i.e., proper) density n_{HI} of neutral hydrogen is

$$d\tau(\lambda) = n_{\text{HI}} \sigma_{\text{eff}}\left(\frac{c}{\lambda}\right) |dl|, \quad (24)$$

where $\sigma_{\text{eff}}(v)$ is defined in Eq. 21. Integrating Eq. 24 along the line-of-sight from source to observer gives the optical depth as a function of observed wavelength λ_{obs} emitted by a source at redshift z_{src} as

$$\tau(\lambda_{\text{obs}}) = \int_0^{z_{\text{src}}} dz \frac{c}{(1+z)H(z)} \bar{n}_{\text{HI}}(z) \sigma_{\text{eff}}\left(\frac{1+z}{\lambda_{\text{obs}}/c}\right) \quad (25)$$

$$\simeq \frac{c \bar{n}_{\text{HI},0}}{\Omega_{\text{m}}^{1/2} H_0} \int_0^{z_{\text{src}}} dz (1+z)^{1/2} x_{\text{HI}}(z) \sigma_{\text{eff}}\left(\frac{1+z}{\lambda_{\text{obs}}/c}\right), \quad (26)$$

where Eq. 5 has been used to change the integration variable from l to z and the second expression uses both the high-redshift $H(z)$ relationship given in Eq. 3 and the cosmological form of the HI density given in Eq. 2.

The fraction of light transmitted is then

$$T(\lambda_{\text{obs}}) = \exp[-\tau(\lambda_{\text{obs}})]. \quad (27)$$

Equation 27 is the basis for the majority of the methods described below to use absorption measurements of quasars to study the reionization history of the Universe.

5 The Gunn-Peterson effect

The Lyman series cross sections are so large near resonance that the IGM would, if even slightly neutral, be all but opaque to all photons with wavelengths of $\lambda \leq \lambda_{\alpha}$. This remarkable fact was discovered independently several times [71, 72, 73, 74], but it was not until Gunn & Peterson [75] presented their calculation, along with measurements [76] of a $z = 2.01$ quasar, that the significance of this result was broadly appreciated, and it is now known almost universally as the Gunn-Peterson (GP) effect.

The opacity of the IGM is independent of the detailed wavelength dependence of the Lyman series resonances (Section 4.1), and can be calculated by adopting the delta function approximation to $\sigma(v)$ given in Eq. 15. The integral in Eq. 25 can then be evaluated directly; converting from observed wavelength to absorption redshift according to $z_n = \lambda_{\text{obs}}/\lambda_{1,n} - 1$ gives the GP optical depth associated with the n th Lyman series resonance as

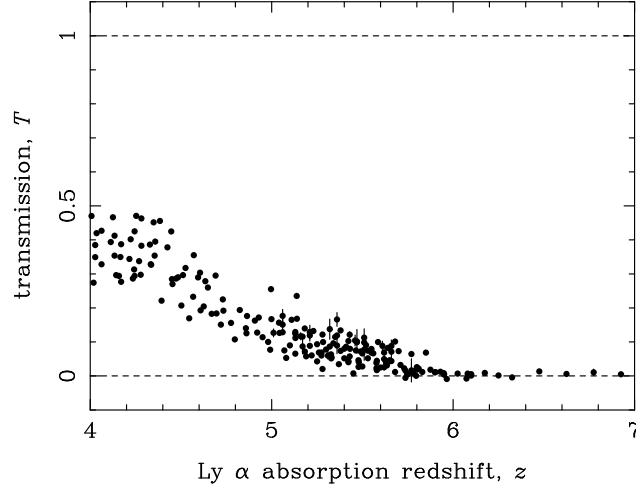


Fig. 5 Measured transmission, \hat{T} , along the lines of sight to HZQs at a range of redshifts [3, 29, 43, 70], shown as a function of Ly α redshift, $z = \lambda_{\text{obs}}/\lambda_{\alpha} - 1$.

$$\tau_{\text{GP},n}(z_n) = \frac{\pi^2 c^2 \sigma_{\text{T}} f_{1,n}^2 \bar{n}_{\text{HI}}(z_n)}{\lambda_{1,n} \Lambda_{1,n} H(z_n)}. \quad (28)$$

The resultant total optical depth to a source at redshift z is then obtained by the summing over the Lyman series to give

$$\tau(\lambda_{\text{obs}}) = \sum_{n=2}^{\infty} \Theta[(1+z)\lambda_{1,n} - \lambda_{\text{obs}}] \tau_{\text{GP},n} \left(\frac{\lambda_{\text{obs}}}{\lambda_{1,n}} - 1 \right), \quad (29)$$

where the step functions produce a distinctive “saw-tooth” pattern in $\tau(\lambda_{\text{obs}})$ as the different resonances drop out with increasing wavelength (cf. [77, 78]).

Most important is the optical depth that results from the Ly α resonance, both because it is the strongest of the Lyman series transitions and has the longest wavelength (hence being by far the dominant channel by which photons emitted with $\lambda_{\text{em}} > \lambda_{\beta} \simeq 0.1 \mu\text{m}$ are absorbed). Evaluating Eq. 28 for $n = 2$ and adopting the fiducial values for the cosmological parameters from Section 2 then gives

$$\tau_{\text{GP},\alpha}(z) \simeq 3.3 \times 10^5 \frac{H_0}{70 \text{ km s}^{-1} \text{ Mpc}^{-1}} \left(\frac{\Omega_{\text{m}}}{0.3} \right)^{-1/2} \frac{\Omega_{\text{b}}}{0.04} \left(\frac{1+z}{7} \right)^{3/2} x_{\text{HI}}(z). \quad (30)$$

Thus a very low IGM neutral fraction of $x_{\text{HI}} \gtrsim 10^{-5}$ would be sufficient to result in significant absorption; and if $x_{\text{HI}} \gtrsim 10^{-3}$ there would be almost complete absorption of all photons emitted with $\lambda < \lambda_{\alpha}$. The GP effect is hence best suited to probing the

end of reionization, as even deep spectroscopic observations of the brightest sources would only result in lower limits on τ_{GP} and hence x_{HI} (cf. [29, 79]). As conceptually simple as this probe of the IGM is, there are a number of complications that make the interpretation of such continuum transmission measurements somewhat unclear.

One source of ambiguity is in simply estimating the fraction of the flux transmitted, naturally estimated as

$$\hat{T}_n(z) = \frac{\hat{F}_v[(1+z)\lambda_{1,n}]}{F_{\text{intr},v}[(1+z)\lambda_{1,n}]}, \quad (31)$$

where $\hat{F}_v(\lambda)$ is the measured flux density of the quasar and $F_{\text{intr},v}(\lambda)$ is a model of the quasar's intrinsic spectrum. This is usually assumed to be a power-law (e.g., [3]), and while the results are somewhat sensitive to the model adopted [80, 81], the increase of τ_{GP} with z is sufficiently dramatic that the uncertainties in the intrinsic emission do not affect the broad interpretation of the transmission estimates.

A second issue is the possibility that the measured absorption is not entirely due to HI in the IGM. Specifically, line blanketing [77] has been invoked as an explanation for the high absorption towards some HZQs.

Regardless of the cause of the absorption, it has become standard to define the observable effective GP optical depth in terms of the estimated transmission (defined in Eq. 31) as

$$\hat{\tau}_{\text{GP,eff}}(z) = -\ln[\hat{T}(z)]. \quad (32)$$

In the high- τ limit this quantity has awkward statistical properties, even being undefined if $\hat{T}(z) \leq 0$, but it is a good summary provided it is evaluated over a sufficiently broad spectral range that non-zero flux is detected. Figure 5 illustrates the observed evolution in the observed transmission with redshift, and also that there is significant variation between different lines-of-sight.

At redshifts of $z \lesssim 5$ the dominant Ly α absorption is in the form discrete HI concentrations that are associated with collapsed objects and seen as the Ly α forest. The level of the continuum between these absorption lines can then be used to estimate – or at least place limits on – the GP optical depth, although the distinction between continuum/IGM and halos/clouds is somewhat artificial (e.g., [82]). Still, this technique has usefully been applied to increasingly distant quasars, yielding, e.g., $\tau_{\text{GP,eff}} \lesssim 0.05$ at $z \simeq 4$ [83, 84], $\tau_{\text{GP,eff}} \simeq 0.1$ at $z = 4.8$ [85], and $\tau_{\text{GP,eff}} \simeq 0.4$ at $z = 5.5$ [86]. At higher redshifts the Ly α forest lines overlap to the degree that identifying regions of continuum emission becomes impractical.

The most comprehensive source of information about the IGM optical depth at $z \simeq 6$ comes from the 19 bright $5.7 \lesssim z \lesssim 6.5$ analysed by Fan et al. [3]. The marked increase in $\hat{\tau}_{\text{GP,eff}}$ with z beyond that which would be expected from the increase in proper density is generally taken as a clear identification of the tail-end of the cosmological reionization, although this conclusion does rest on a number of assumptions about the distribution of HI in the IGM and the ionizing background (cf. [87, 88]).

At redshifts of $z \gtrsim 6$, the density of H I was sufficiently high that $\tau_{\text{GP}} \gg 1$, meaning that almost all light blueward of Ly α is absorbed. The GP effect cannot be exploited to measure x_{HI} deep into the reionization epoch, as it is only possible to place lower limits on τ_{GP} and x_{HI} . To probe further – at least using quasars – requires going beyond the average properties of the IGM (as encoded by the optical depth) and exploiting its structure (Section 5.1), the distribution of transmission values (Section 5.2), or the comparatively weak red damping wing of the Ly α transition (Section 7).

5.1 Dark gaps

If, at a given redshift, the neutral fraction of the hydrogen in the IGM was $x_{\text{HI}} \gtrsim 0.01$ then almost all photons emitted with $\lambda < \lambda_{\alpha}$ from sources at or beyond this redshift would be absorbed. As discussed in Section 5, the resultant GP optical depth measurements cannot be used to do anything more than place upper limits on x_{HI} . One alternative ([89, 90, 91]), is to instead look at the lengths of the GP troughs, by applying what has become known as a dark gap analysis.

Assuming the reionization process is patchy, it is expected that even at times when the Universe was still fairly neutral there would be small highly-ionized regions (e.g., [92]), which might be seen as sharp “spikes” of transmission in the spectra of HZQs. (Early in the reionization process it is possible that the even highly ionized regions have a sufficient residual density of H I to be opaque to Ly α photons, and the spatial fluctuations in the ionizing background [43] further complicate this issue.) There is expected to be more information in the positions of these spikes – and, in particular, the separations between them – than can be encoded by simply folding them into an optical depth measurement. Between these transmission peaks would be long regions with no detectable flux; these dark gaps are expected to be longer at higher redshifts when the IGM was more neutral and so could be the extreme version of the GP troughs discussed in Section 5, and are often referred to as dark gaps. The potential importance of dark gaps lies in the possibility that their number and length might be both observable and sensitive probes of the ionization state of the IGM; to date, however, it has proved difficult to convert this appealing idea into quantitative constraints on the cosmological reionization history.

One difficulty in all dark gap studies is that the definition is, unlike that of, e.g., the GP optical depth, dependent on the observation under consideration. The identification of a transition spike, which would hence break a long dark gap into two shorter gaps, does not necessarily correspond to real transmission, and so this technique cannot be completely disentangled from the noise level and resolution of the spectrum being analysed. Particularly in the case of $z \gtrsim 7$ sources, the residual presence of sky lines in the relevant wavelength range (e.g., [29]) means dark gap statistics are subject to a very complicated source of noise. In more concrete terms, two different observations of the same quasar could easily yield very different dark gap numbers and lengths, implying that these statistics are not robust.

Observations of redshift $\lesssim 5$ quasars showed increasing absorption due to isolated concentrations of H I, but the first detection [93] of an extended region of high absorption was in the $z = 5.74$ quasar SDSS J1104–0125, for which $\tau_{\text{GP,eff}} > 4.6$ over the redshift range $5.2 \lesssim z \lesssim 5.6$. This was not, however, unequivocal evidence of an increase in the IGM neutral fraction as line blanketing (cf. Section 5) could also result in long sections of minimal transmission from a region of IGM that was mostly, by volume, ionized [90]. Subsequent observations of the $z = 6.30$ quasar SDSS J1030+0524 [94] and the $z = 6.42$ quasar SDSS J1148+5251 [7] revealed even longer dark gaps, spanning the redshift ranges $6.0 \leq z \lesssim 6.26$ [8, 94] and $6.1 \leq z \lesssim 6.30$ [8], respectively. The expected increase in gap length with redshift was confirmed by the $z = 7.08$ quasar ULAS J1120+0641 [29], which shows no detectable Ly α transmission above $z \simeq 5.8$, albeit from a noisier spectrum than those available for SDSS J1030+0524 and SDSS J1148+5251. (There is also no emission detected blueward of the Ly α lines of the three $z > 6.5$ quasars discovered in VISTA [40], although the spectra published to date are noisier again.)

While there is a clear trend with redshift, there is also significant variation between lines-of-sight (e.g., [3]), as shown most strikingly by the discovery [43] of a $\tau_{\text{GP,eff}} > 7$ trough covering the redshift range $5.5 \lesssim z \lesssim 5.9$ in the $z = 5.98$ quasar ULAS J0148+0600 [42]. The strongest inference that can be made from these observations is that reionization was an extremely inhomogeneous process, counselling against making any strong inferences from measurements along a single line-of-sight.

Moving from the qualitative result that the dark gap lengths increase with redshift to quantitative constraints on the neutral fraction has also proved difficult. In principle, the best option would be to compare the gap distribution with the predictions of numerical models [95, 96, 97], but great care must be taken to avoid making strong conclusions that are tied to assumptions about the spatial distribution of hydrogen and the ionizing background. Partly for this reason, the promised quantitative constraints on the neutral fraction have not been forthcoming; but dark gaps might become more important as spectra are obtained of quasars deeper into the reionization epoch.

5.2 Dark pixels

Another way to exploit the almost complete absorption produced by regions of H I is to look at the fraction of of a HZQ spectrum for which there is no (detectable) transmission. The key point here is that the transmission distribution is, by virtue of its exponential relationship to the H I density, strongly skewed to values close to zero; with the addition of observational noise there is a 50% chance that any such pixels will have negative measured transmission.

It has been argued [4, 88] that dark gap statistics provide the most model-independent constraints on the neutral fraction, especially towards the end of reionization. The inevitable price is a loss in precision, a result of discarding a large

amount of the information contained in the observed transmission profiles, but in such a complicated setting reliability is to be valued. The most extreme version of this trade-off is to estimate the number of dark pixels as twice the number of pixels with negative measured fluxes (e.g., [4]). Applying this methodology to 22 redshift ~ 6 quasar spectra gave $x_{\text{HI}} \leq 0.06 \pm 0.05$ at a redshift of 5.9, robust additional evidence that reionization was close to complete by $z \simeq 6$. [98].

6 Quasar H II regions

Quasars are not only passive probes of the H I density, but also partial causes of reionization, as they emit a significant numbers of ionizing photons⁶. While massive stars in ordinary galaxies were the dominant contributors to global reionization (e.g., [99, 100]), quasars can have a dramatic effect on their local environment, being capable of creating Mpc-scale H II regions⁷ in an otherwise neutral IGM. While the stars in galaxies can also produce H II regions, those produced by quasars are considerably larger than expected from an individual galaxy [102] or even a proto-cluster [103]. Towards the end of reionization the ionizing background from numerous more distant sources can be comparable to the radiation even close to a quasar, so the focus here is on H II regions produced by quasars when reionization was still complete.

Assuming that the quasar is the dominant local source of (isotropically emitted) ionizing photons, and that the surrounding IGM is uniform, the (proper) radius of the spherical H II region, R_{HII} , evolves according to [102, 104, 105]

$$\frac{dR_{\text{HII}}}{dt} = \frac{\Gamma_{\text{ion}}}{4\pi R_{\text{HII}}^2 \bar{n}_{\text{HI}}} + H R_{\text{HII}} - \bar{n}_{\text{HI}} \alpha_{\text{B}} R_{\text{HII}}, \quad (33)$$

where H is the (time-dependent) Hubble parameter, Γ_{ion} is the rate at which the quasar was emitting ionizing photons, and $\alpha_{\text{B}} \simeq 2.6 \times 10^{-19} \text{ m}^3 \text{ s}^{-1}$ is the case B hydrogen recombination coefficient (with the value quoted appropriate for an IGM temperature of $\sim 10^4$ K). The first term on the right-hand side of Eq. 33 corresponds to the production of ionizing photons by the quasar; the second corresponds to the expansion of the H II region with the Hubble flow, which can be ignored if the age of the quasar when observed, T_{q} , is much less than the Hubble time (at the redshift in question); the third term corresponds to recombinations within the H II region, and should be unimportant at redshifts of $\lesssim 10$. Making these approximations leads

⁶ Here ionizing photons are those with an energy of $E > 13.6 \text{ eV} = 2.18 \times 10^{-18} \text{ J}$, or a wavelength of $\lambda < 0.0912 \text{ } \mu\text{m}$, sufficient to remove a ground state electron from a hydrogen atom.

⁷ The H II region formed by a quasar surrounded by a predominantly neutral IGM is similar to a classical Strömgren sphere formed by an O or B star [101]. The main difference is that a Strömgren sphere is static, the continuous emission of ionizing radiation being balanced by recombinations in the inter-stellar medium, whereas the density of the IGM during reionization is so low that the H II region around a high-redshift quasar can be expected to grow for the entirety of the quasar's lifetime.

to the simple result that the R_{HII} can be approximated by equating the number of ionizing photons that had been emitted by the quasar at the time it was observed⁸ with the number of neutral hydrogen atoms in a volume $4\pi R_{\text{HII}}^3/3$ of the IGM at that redshift, which gives (cf. [102, 107, 108])

$$R_{\text{HII}} = \left[\frac{3 T_{\text{q}} \Gamma_{\text{ion}}}{4\pi \bar{n}_{\text{H},0} (1+z)^3 x_{\text{HI}}(z)} \right]^{1/3} \quad (34)$$

$$\simeq 8.0 \left(\frac{\Gamma_{\text{ion}}}{6.5 \times 10^{57} \text{ s}^{-1}} \right)^{1/3} \left(\frac{T_{\text{q}}}{2 \times 10^7 \text{ yr}} \right)^{1/3} \left(\frac{1+z}{7} \right)^{-1} x_{\text{HI}}^{-1/3}(z) \text{ Mpc}, \quad (35)$$

where Eq. 2 has been used to exhibit the dependence on the neutral fraction and z is the redshift of the quasar. More realistic calculations of R_{HII} have included effects such as departures from spherical symmetry, over-densities inside the H II region, and fluctuations in quasar luminosity (e.g., [8, 109, 110, 111, 112]), but the scaling of R_{HII} with the number of ionizing photons and the local density of H I is reasonably generic.

This leads to the appealing possibility of using the measured H II region sizes of HZQs as a tracer of the evolving neutral fraction, although the various attempts to do so (e.g., [106, 110, 111, 113, 114, 115, 116, 114]) have produced results that are at odds with other probes – and, in some cases, contradict each other. Most of these problems stem from the difficulty of estimating R_{HII} from line-of-sight absorption measurements (Section 6.1); in the future more progress might be made with observations in the plane of the sky to obtain direct images of HZQ H II regions (Section 6.2).

6.1 Near zone measurements

The only currently practical option for measuring R_{HII} around a HZQ is to exploit the fact that the presence of H II in front of a quasar results in a near zone (NZ) of significant transmission just blueward of each Lyman series emission line⁹. Examples of observed NZ transmission profiles towards some HZQs are shown in Fig. 6.1. If the H II region around a quasar at redshift z_{src} was completely ionized then there would be a region of complete transmission just blueward of the n th Lyman series transition, extending to a wavelength of (cf. Eq. 7)

⁸ The fact that the ionization front grows at an appreciable fraction of the speed of light implies that care must be taken when calculating the time that the quasar has been emitting ionizing radiation; but the fact that the observed photons and the ionizing photons take the same time to reach the edge of the NZ leads to an exact cancellation in the case of the line-of-sight observations discussed in Section 6.1 [8, 106].

⁹ The physical processes that produce a quasar NZ at $z \gtrsim 6$ are the same as those responsible for the proximity effect (e.g., [117]) in lower redshift quasars.

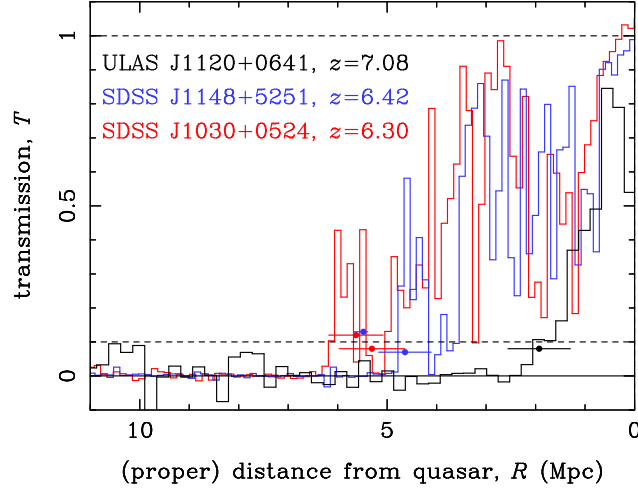


Fig. 6 The NZ transmission profiles of three HZQs, as labelled, showing both the systematic evolution with redshift and the complicated H I distribution along individual lines-of-sight. The very different noise levels of the three spectra can be gauged from the fluctuations at distances of $R \gtrsim 6$ Mpc as the IGM is essentially opaque, resulting in $T = 0$, in front of these sources. The dashed line at $T = 0.1$ corresponds to the value commonly used to estimate R_{NZ} (as described further in Section 6.1). The estimated R_{NZ} values, calculated from the z_{NZ} values in Table 1, are shown just below this line; estimated R_{HII} values [87] are shown just above this line.

$$\lambda_{\text{obs,HII},n} \simeq \lambda_{1,n} (1 + z_{\text{src}}) \left[1 - \frac{R_{\text{HII}}}{c/H_0} \Omega_{\text{m}}^{1/2} (1 + z_{\text{src}})^{3/2} \right]. \quad (36)$$

This wavelength is almost always observable for $n = 1$ (i.e., Ly α) and often for $n = 2$ (i.e., Ly β) as well, but seldom for higher order transitions as the relevant region of the spectrum is typically subject to complete GP absorption (Section 5) at these redshifts.

The most powerful approach to analysing the observed spectra in the wavelength range from $\lambda_{\text{obs,HII},n}$ to $\lambda_{1,n} (1 + z_{\text{src}})$ is to use the transmission measurements to constrain a physical model of the residual H I inside the H II region [113, 118, 119]. In particular, such models have shown that the density of residual H I towards the outside of the H II region can be sufficient to produce an optical depth of $\tau \gg 1$, meaning that the observable NZ of high transmission would not extend all the way to $\lambda_{\text{obs,HII},n}$ [113, 119]. But, as the effects of possible damped absorption from the IGM should also be included in such an analysis, a discussion of this is deferred to Section 7.

The opposite approach, which has the virtue of simplicity, is to characterize the NZ in terms of the wavelength range of significantly positive transmission. The specific definition most commonly used is to define $\lambda_{\text{obs,NZ},n}$ as the observed wave-

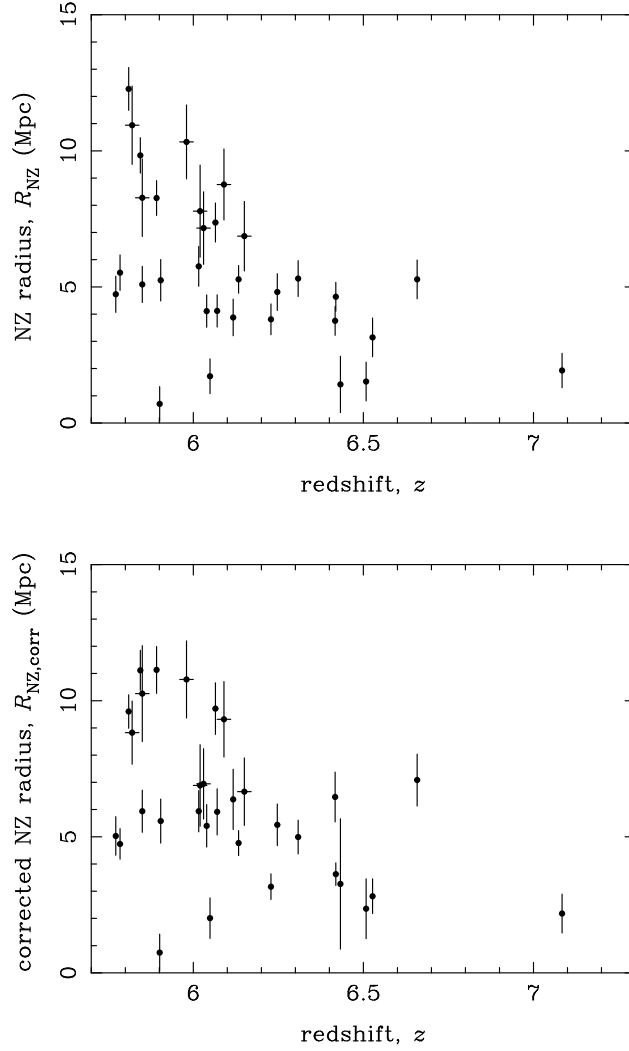


Fig. 7 Estimated proper radii (top panel) and corrected proper radii (bottom panel) of HZQ NZs, calculated using the fiducial cosmological model defined in Section 2 for the quasars with z_{NZ} measurements as listed in Table 1.

length at which the measured transmission, binned on a reasonable but somewhat arbitrary scale of $0.002 \mu\text{m}$, first drops to 10% of its peak value, as measured bluewards from the n th Lyman series emission wavelength [3]. Converting to the transition-independent NZ redshift, $z_{\text{NZ}} = \lambda_{\text{obs,HII},n} / \lambda_{1,n} - 1$, then allows R_{NZ} to be estimated by inverting Eq. 6 to give

$$R_{\text{NZ}} \simeq \frac{c}{H_0} \frac{z_{\text{src}} - z_{\text{NZ}}}{\Omega_{\text{m}}^{1/2} (1 + z_{\text{src}})^{5/2}}. \quad (37)$$

The observational uncertainty in z_{NZ} is typically $\sigma_{\text{NZ}} \simeq 0.01$ [3, 33]; the uncertainty in the systemic source redshift, z_{src} , depends primarily on how it has been estimated from the observed spectrum. The least accurate, but most widely available, option is to use the red wing of the Ly α emission line, combined with the often blended N V emission line (rest-frame wavelength $\lambda = 0.1240 \mu\text{m}$), for which $\sigma_{\text{src}} \simeq 0.02$, although the fact that this is not separate from the spectral break is problematic for making meaningful NZ measurements. It is far more reliable and precise to base systemic redshifts on the Mg II emission line (rest-frame wavelength $\lambda = 0.2798 \mu\text{m}$), which gives $\sigma_{\text{src}} \simeq 0.007$ (e.g., [33, 120]), or the narrower mm-band molecular CO features, which can yield $\sigma_{\text{src}} \lesssim 0.002$ (e.g., [33, 52, 121]). By comparison, $R_{\text{HII}} \simeq 5 \text{ Mpc}$ at $z_{\text{src}} = 6$ gives $z_{\text{src}} - z_{\text{NZ}} \simeq 0.1$, implying that the resultant R_{NZ} measurements are at least statistically meaningful – but this does not imply that R_{NZ} is a good proxy for R_{HII} .

All the published measurements of z_{src} and z_{NZ} for $z_{\text{src}} \geq 5.8$ quasars are tabulated in Table 1. The resultant estimates of both the actual NZ radius, R_{NZ} , and the luminosity-corrected NZ radius¹⁰, $R_{\text{NZ,corr}}$, are plotted against z_{src} in Fig. 7. A clear anti-correlation is apparent, implying that the IGM was in a significantly different state at $z \simeq 6$ than it had been $\sim 10^8 \text{ yr}$ earlier at $z \simeq 7$. But it is difficult to make more quantitative statements, due in part to the scatter that results from the range of intrinsic quasar properties (mainly age at time of observation) and environment (the density and distribution of hydrogen in the surrounding IGM), but largely because R_{NZ} is significantly lower than R_{HII} in general. It is hence unlikely that HZQ NZ measurements will prove to be the accurate probe of the cosmological reionization history that was initially hoped for, although they will continue to be measured as a natural fringe benefit of obtaining accurate systemic HZQ redshifts.

6.2 Imaging

A strong validation of the overall reionization paradigm would be if an HZQ H II region could be imaged directly, rather than just inferred from a spectroscopic absorption profile. An H II region of (proper) radius $\sim 5 \text{ Mpc}$ at $z = 6$ would have an angular radius of $\sim 0.2 \text{ deg}$, resolvable using current instruments at most wavelengths. The choice of wavelength is key, however, as it there must be some emission

¹⁰ Equation 34 makes it clear that estimates for both Γ_{ion} and T_{q} are needed if any attempt is to be made to infer x_{HII} from the scale of either the NZ or the H II region. It is at least plausible to assume that the ionization rate is proportional to the quasar’s luminosity, L , at the moment of observation, leading to the use of the “corrected” NZ radius [3] $R_{\text{NZ,corr}} = R_{\text{NZ}} 10^{2/5[M_{1450} - (-27)]/3} \propto R_{\text{NZ}}/L^{1/3}$, defined so that quasars of different luminosities can be compared on an approximately equal footing.

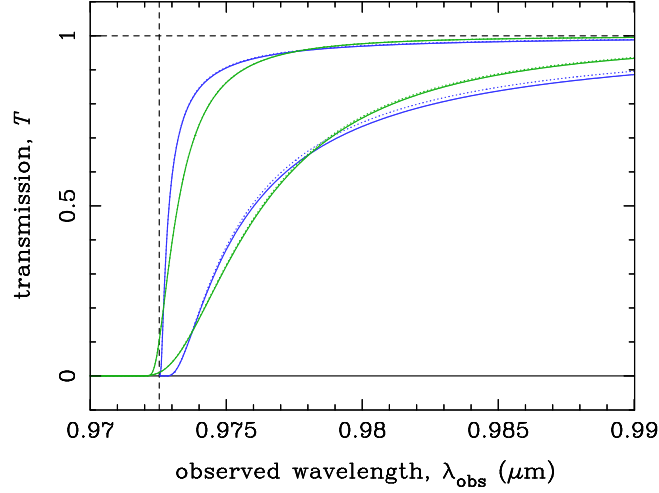


Fig. 8 Damped Ly α transmission profiles as produced by extended IGM absorption (blue) and a DLA (green). The IGM profiles are for the default cosmological parameters in Section 2 with constant neutral fractions of $x_{\text{HI}} = 0.1$ (top) and $x_{\text{HI}} = 1.0$ (bottom) between $z_{\text{start}} = 7.0$ and $z_{\text{end}} = 6.0$. The vertical dashed line indicates the wavelength of Ly α at $z = 7.0$. The DLA profiles are matched to these, with $\Sigma_{\text{HI}} = 6.0 \times 10^{23} \text{ m}^{-2}$ at $z_{\text{abs}} = 6.993$ for the $x_{\text{HI}} = 0.1$ model and $\Sigma_{\text{HI}} = 1.0 \times 10^{25} \text{ m}^{-2}$ at $z_{\text{abs}} = 6.980$ for the $x_{\text{HI}} = 1.0$ model. All curves are paired, showing the results for the Lorentzian line profile (solid) and the two-level line profile (dotted); these are not always distinguishable.

(or absorption) signature by which the NZ is to be distinguished from its surroundings.

One promising possibility is collisional excitation of the residual H I in the H II region which could be seen in an appropriately tuned filter [122]. This effect is stronger with a higher neutral fraction, and so the most promising targets for observation are the most distant known quasars – a High Acuity Wide field K-band Imager (HAWK-I [123]) program to observe ULAS J1120+0641 at $z = 7.08$ is currently underway.

In the longer term, radio observations of redshifted 21 cm emission from – and absorption by – H I should yield direct images of large numbers of HZQ H II regions [111, 124].

7 The Ly α damping wing

If the IGM in front of a source was mostly neutral then there would be appreciable absorption redward of the wavelength of Ly α photons leaving the quasar’s H II

region (Section 6), and possibly reward of the systemic Ly α emission wavelength as well. This comes about due to the sum of the Rayleigh scattering wings, which combine to give the long wavelength damped absorption seen clearly in Figs 3 and 7.

The mere detection of such a damping wing would, provided it could be shown that it did not arise from a discrete concentration of H I, be direct evidence that $x_{\text{HI}} \gtrsim 0.1$. Further, as the depth and extent of the damping wing are determined by the density of H I in front of the source, the observed transmission profile could be used to measure x_{HI} in front of the source. The fact that the damping wing is many orders of magnitude weaker than the resonant absorption that produces the GP effect (Section 5) makes it a potentially useful probe of redshifts at which the hydrogen in the IGM is completely neutral. Conversely, there is also information to be gleaned from the absence of a detectable damping wing, as this places an upper limit on the H I density in front of a source. Any such constraint is robust to the presence of a discrete H I concentration: the upper limit on x_{HI} could only be made stronger as a result.

7.1 IGM absorption profile

The canonical IGM damping profile is calculated by adopting the simple model that x_{HI} was constant between the front of any H II region around the source (Section 6), at redshift z_{start} , and the hard end-point of reionization, at redshift z_{end} . Inserting this simple reionization history into Eq. 25 gives the optical depth at an observed wavelength of $\lambda_{\text{obs}} > (1 + z_{\text{start}}) \lambda_{\alpha}$ as (cf. [64, 125])

$$\tau(\lambda_{\text{obs}}) = \frac{c \bar{n}_{\text{H},0} \sigma_{\text{T}} f_{1,2}^2 x_{\text{HI}}}{\Omega_{\text{m}}^{1/2} H_0} \left(\frac{\lambda_{\text{obs}}}{\lambda_{\alpha}} \right)^{3/2} \left\{ I \left[\frac{(1 + z_{\text{start}}) \lambda_{\alpha}}{\lambda_{\text{obs}}} \right] - I \left[\frac{(1 + z_{\text{end}}) \lambda_{\alpha}}{\lambda_{\text{obs}}} \right] \right\}, \quad (38)$$

where

$$I(x) = \int dx x^{1/2} \frac{\sigma(x v_{\alpha})}{\sigma_{\text{T}} f_{1,2}^2} \quad (39)$$

is the dimensionless integral that results from changing the integration variable from z to $x = v/v_{\alpha} = (1 + z) \lambda_{\alpha}/\lambda_{\text{obs}}$. In contrast to GP absorption (Section 5), there is no meaningful conversion from λ_{obs} to z , as the flux received at any given wavelength is gradually attenuated as it passes through the IGM.

The strength of the absorption at the redshifted Ly α wavelength can be gauged by comparison to the GP optical depth given in Eq. 28: identifying $\lambda_{\text{obs}}/\lambda_{\alpha}$ as z_{src} , the pre-factor in Eq. 38 can be re-written as $2 \Lambda_{1,2} \lambda_{\alpha}/(3c) \tau_{\text{GP},\alpha}(z_{\text{src}}) \simeq 10^{-7} \tau_{\text{GP},\alpha}(z_{\text{src}})$. It is this comparative weakness of the damping wing absorption that makes it a potentially useful probe of a largely neutral IGM.

If the full cross section from Eq. 11 is used then the integration must be evaluated numerically, but a good combination of simplicity and accuracy ($\sim 1\%$ relative

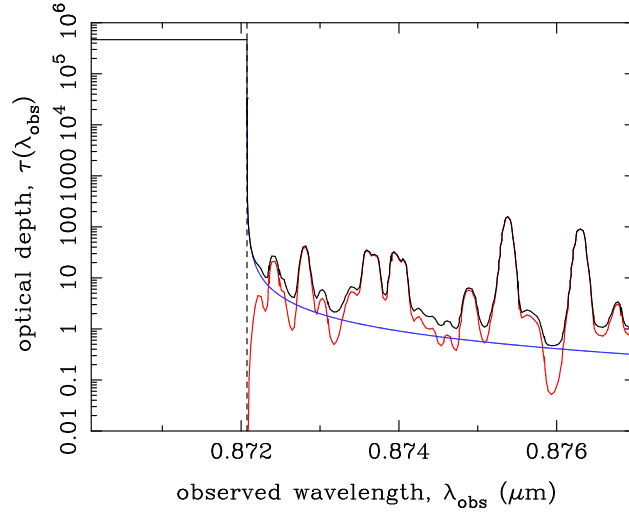


Fig. 9 The optical depth along a typical line-of-sight towards a quasar at $z = 6.28$ (such as SDSS J1030+0524). The quasar is assumed to be embedded in a fully neutral, smooth IGM, but surrounded by a H II region with a (proper) radius of $R = 6$ Mpc. The red curve shows the contribution from residual H I inside the H II region; the blue curve shows the contribution from H I outside the H II region in the surrounding IGM; the black curve shows the total optical depth, given by the sum of these two contributions. The vertical dashed line indicates the edge of the H II region. For reference, the redshifted Ly α emission wavelength is at $0.8852 \mu\text{m}$, far to the right off the plot. Adapted from [113].

error) can be achieved by using the simple Lorentzian form of $\sigma(\nu)$ given in Eq. 14. This yields

$$I_{\text{Lor}}(x) \simeq \int dx \frac{x^{1/2}}{4(x-1)^2} = \frac{x^{1/2}}{4(1-x)} + \frac{1}{2} \ln \left(\frac{1-x^{1/2}}{1+x^{1/2}} \right) \quad (40)$$

and gives the IGM damping wing profiles shown as the solid curves in Fig. 7. Using the two-level model from Eq. 19 gives the widely used result that (cf. [64])

$$\begin{aligned} I_{2\text{L}}(x) &\simeq \int dx \frac{x^{9/2}}{4(x-1)^2} \\ &= \frac{x^{1/2}(315 - 210x - 42x^2 - 18x^3 - 10x^4)}{140(1-x)} + \frac{9}{8} \ln \left(\frac{1-x^{1/2}}{1+x^{1/2}} \right), \quad (41) \end{aligned}$$

shown as the dotted curves in Fig. 7. Even though the cross section of the two-level model is too low by a factor of ~ 10 in the long-wavelength limit (Section 4.1), most of the absorption occurs when the photons first enter the IGM, the regime in which

the discrepancy is smallest. Hence the two-level IGM transmission profile underestimates the absorption by $\lesssim 5\%$, although the Lorentzian – or a more accurate approximation [61, 63] – should be used in its place.

While it is an important point of principle to use an appropriate form of the wavelength-dependent cross section in any calculation of the IGM damping wing, there are several limitations of the simple model above that can have at least as much impact on the transmission profile:

- The IGM is not uniform in density, and so the clumped residual H I inside the H II region around a quasar can produce a transmission signature like that of the Ly α forest [87, 114, 118, 119, 126].
- The H II region of a quasar will contain other ionizing sources (i.e., galaxies), which contribute to the local ionization balance. The relative importance of these galaxies increases with distance from the quasar, and is hence greatest close to the edge of the H II region (e.g., [127]).
- Quasars are expected to be biased, and so will reside in overdensities of galaxies and gas on a scale of a few Mpc [106, 128, 129]. The effects of increased ionizing radiation would tend to be cancelled out by the extra gas, and so detailed simulations are required to assess whether the net effect is significant.
- The interior of the H II region can become optically thick to ionizing radiation, necessitating a full radiative transfer calculation (e.g., the quasar’s flux will drop more rapidly than with the square of distance from the quasar [130, 131]). Describing the distribution of optically thick clumps (i.e., “Lyman limit systems”) near the quasar is one of the largest, and most challenging, modeling uncertainties [132].
- In addition to the nonuniform density, the IGM outside the H II region is ionized in patches, rather than uniformly [133], which will make the wavelength-dependence of the damping wing differ from the above uniform IGM model [119, 134, 135, 69]. Simulations indicate that there is significant bias in the inferred reionization parameters if this effect is not taken into account [136, 137].

One approach to dealing with these issues is to use numerical simulations of the H I distribution around a HZQ (e.g., [113, 118, 119]). The results of this approach are illustrated in Fig. 7.1, showing the separate contributions of the H I inside and outside the H II region towards a fiducial HZQ. As can be seen, the contributions from the two distinct components are significant; both can be accounted for in a pixel optical depth analysis as discussed further in Section 7.3 below.

7.2 DLA profile

A high column density H I cloud in front of a source would also produce damped absorption that, given realistic observational uncertainties, could be effectively indistinguishable from an IGM damping wing. Assuming the local IGM has $x_{\text{HI}} \gtrsim 10^{-4}$, the GP absorption blueward of the NZ edge would leave just the red damping wing

(as distinct from a DLA in an ionized medium, for which both wings of the Ly α line are often seen). The proper density of an a thin H I cloud of column density Σ_{HI} at a redshift of z_{abs} can be approximated as

$$\bar{n}_{\text{HI}}(z) = \frac{(1+z)H(z)\Sigma_{\text{HI}}}{c} \delta_{\text{D}}(z - z_{\text{abs}}), \quad (42)$$

where the line element from Eq. 5 has been used to change the argument of the delta function from the local line-of-sight spatial coordinate to redshift. Inserting this into Eq. 26 then gives the standard DLA optical depth

$$\tau(\lambda_{\text{obs}}) = \Sigma_{\text{HI}} \sigma_{\text{eff}} \left(\frac{1 + z_{\text{abs}}}{c/\lambda_{\text{obs}}} \right), \quad (43)$$

where $\sigma_{\text{eff}}(v)$ is the velocity-convolved effective cross section defined in Eq. 21. If line-of-sight velocities are unimportant (e.g., significantly redward of resonance) then the Lorentzian cross section from Eq. 14 can be used to give

$$\tau(\lambda_{\text{obs}}) \simeq \frac{\Sigma_{\text{HI}} \sigma_{\text{T}} f_{1,2}^2}{4[(1 + z_{\text{abs}}) \lambda_{\alpha}/\lambda_{\text{obs}} - 1]^2}, \quad (44)$$

which is compared to the IGM transmission profiles in Fig. 7. (If velocities are important then the more complicated Voigt profile given in Section 4.2 should be used.)

The similarity between the tuned DLA profile and the IGM profiles shown in Fig. 7 is such that it will require exquisite quality spectra to distinguish between them on the basis of data alone [63, 64, 135, 138], although there are other approaches to tackling this problem, as discussed below.

7.3 Observational issues

The challenges of identifying and interpreting damped IGM absorption towards a distant quasar are not limited to the theoretical issues described above: there are significant observational challenges as well, both blueward and redward of the quasar's systemic Ly α wavelength.

Any damped absorption would be strongest at the front edge of the H II region around the quasar; and, assuming a canonical (proper) radius of ~ 5 Mpc (Section 6), it is only blueward of the systemic Ly α wavelength that an IGM damping wing would be visible if $x_{\text{HI}} \lesssim 0.1$, and it is hence in this wavelength range that searches for damped absorption towards $z \lesssim 6.5$ quasars have concentrated to date. The main complication is the need to model the effects of the residual H I inside the quasar's H II region, as discussed in Section 7.1, with uncertainty in the quasar's intrinsic emission a secondary issue [130]. The results of these pixel optical depth studies are inevitably strongly model-dependent, although the fact that the

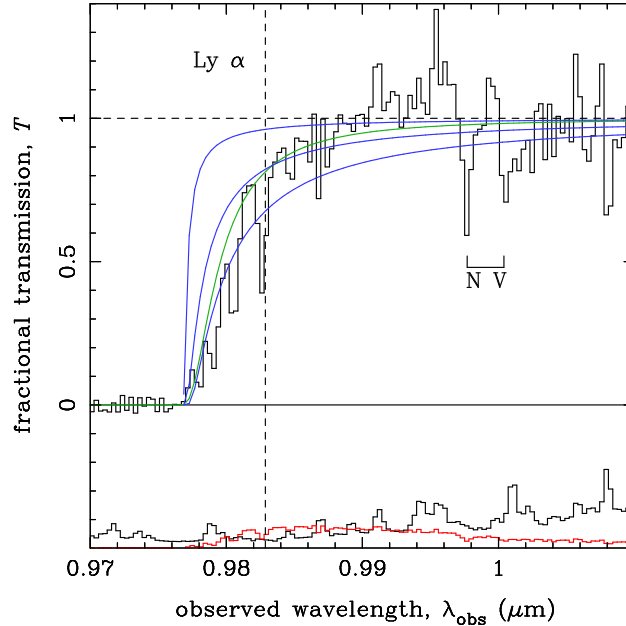


Fig. 10 Estimated transmission towards the $z = 7.08$ quasar ULAS J1120+0641 obtained by dividing the observed spectrum by a model for its intrinsic emission based on lower redshift quasar spectra [29]. The resultant systematic uncertainty is shown at the bottom in red, along with the observational noise in black. Shown in blue are theoretical IGM damping wing profiles for the default cosmological parameters in Section 2 with constant neutral fractions of $x_{\text{HI}} = 0.1$, $x_{\text{HI}} = 0.5$ and $x_{\text{HI}} = 1.0$ (from top to bottom) between $z_{\text{start}} = 7.035$ and $z_{\text{end}} = 6.0$. A DLA profile is shown in green for an H I cloud of column density $\Sigma_{\text{HI}} = 4 \times 10^{24} \text{ m}^{-2}$ at $z_{\text{abs}} = 7.025$. (These curves differ slightly from those shown in [29] due to the use of the Lorentzian line profile and the inclusion of a helium fraction of $Y = 0.24$.)

residual H I should also show the same transmission pattern blueward of the Ly β line can provide an important check [113]. Applying this approach to three bright $6.2 < z < 6.5$ SDSS quasars implied that $x_{\text{HI}} \simeq 1$ at $z \simeq 6$ along two of these lines-of-sight [87]; a subsequent improved analysis [69] updated these constraints to be $x_{\text{HI}} \gtrsim 0.1$.

The most unambiguous detection of damped absorption would be if it could be confirmed redward of the quasar’s systemic Ly α wavelength, as it is only the damping wing absorption from cosmological H I patches (and/or a possible a DLA) that need be taken into account – the (uncertain) distribution of residual H I would not have a significant effect and could be ignored. The main difficulty is that an estimate of the fractional transmission – and particularly its wavelength dependence – requires an accurate model of the unabsorbed spectral energy distribution of the

quasar, specifically the strong Ly α +N v emission lines¹¹. Plausible results can be obtained by fitting a parameterised model spectrum (e.g., [113]), but the fact that the properties of quasars' Ly α +N v lines are correlated with the unabsorbed emission at longer wavelengths (e.g., [120]) should be exploited if possible.

This approach has been applied to the $z = 7.08$ quasar ULAS J1120+0641, which does appear to exhibit absorption redward of Ly α [29], as shown in Fig. 7.3, although this view is not unanimously held [141]. Despite significant systematic uncertainties from the inevitable ignorance about the quasar's true emission, the identification of absorption redward of Ly α is supported by completely independent data and analysis methodology [142]. There is, however, the remaining question of whether the absorption is due to the IGM (which would imply $x_{\text{HI}} \gtrsim 0.1$ at $z \simeq 7$) or a DLA (with a very high column density of $\Sigma_{\text{HI}} \simeq 10^{24} \text{ m}^{-2}$). Simulations of the H I distribution in such systems imply that such isolated concentrations are rare, being expected along only one line-of-sight in ~ 20 [116]; and, given also that numerical simulations imply such pristine gas would not last to that epoch [143], the lack of any associated metal absorption lines [142] also disfavors the DLA hypothesis. It is also tempting to try and interpret the shape of the damped profile, although to do this correctly will require that the impact of patchy ionization in the IGM and residual H I in the H II region be accounted for.

An obvious approach to verifying and extending these results would be to apply the same analysis to the more recently discovered $z \gtrsim 6.5$ quasars [30, 40]. These sources have not yet been analysed in great detail, but the necessary high signal-to-noise ratio spectroscopic observations will presumably be made in due course. Another way of making progress here, particularly on the IGM vs. DLA question, would be by finding more bright $z \simeq 7$ quasars: if damping wings were rare then the implication would be that the IGM was fairly ionized at this epoch; if damping wings were ubiquitous then it would be unequivocal that the IGM was significantly neutral.

8 Future observational prospects

A recurring theme above is that more bright quasars with redshifts of $z \gtrsim 6$ need to be identified to establish the global evolution of the hydrogen in the IGM. In terms of numbers, the Dark Energy Survey (DES [144]) and Pan-STARRS should soon eclipse SDSS and the CFHQS, after which the Large Synoptic Survey Telescope (LSST [145]) will, from its first scans, be able to complete the census of quasars with $z \lesssim 6.5$. All these surveys only extend to the Y band, which will limit their ability to explore higher redshifts without complementary NIR data.

The fact that there are currently only seven confirmed optical drop-out quasars with $z \gtrsim 6.5$ means that there is still considerable amount to be done with NIR-based quasar searches, to at least provide a sample that can be compared with

¹¹ This is not an issue with GRBs, which have very smooth spectra at these wavelengths (e.g., [138, 139, 140]).

the optically-selected $z \lesssim 6.5$ objects. Unfortunately, this is likely to be considerably more challenging than merely “repeating” SDSS-like searches at longer wavelengths: the quasar luminosity function decreases with redshift as $\sim 10^{-0.5z}$ [14] and so the level of contamination by Galactic stars and brown dwarfs will increase accordingly. Still, progress will be made here, even if slowly [15]: two $z \gtrsim 6.5$ quasars have been detected in UKIDSS; and VISTA will yield more sources at comparable distances. Both surveys have sufficient wavelength coverage that they could also probe $z \gtrsim 8$, although their area coverage is such that it is possible that neither will yield such Y -band drop-out quasars. Further ahead, Euclid [146] should revolutionise this field due to its large ($\sim 20,000 \text{ deg}^2$) area coverage and comparatively deep NIR imaging. There is also the possibility that Euclid will find HZQs using low-resolution spectroscopy [78].

Finding new and more distant quasars with these surveys will, however, only be useful for probing reionization if it is possible to obtain deep spectroscopic observations of these objects, so there is a trade-off between area and depth. Given that the ultimate observational aim – to have accurate absorption measurements along many lines-of-sight – is essentially the same, which of these two options can be most usefully pursued depends in part upon the resources available. For instance, both the Thirty Metre Telescope (TMT) and Giant Magellan Telescope (GMT) ought to be able to obtain spectra of all the known HZQs that are comparable in quality to those which are currently available only for, e.g., SDSS J1148+0521 [8]. Conversely, the decreased pressure on smaller telescopes like those used for the SDSS and UKIDSS projects might make it possible to greatly increase the area covered by these types of surveys, potentially yielding HZQs a magnitude or more brighter than those known at present.

The next decade should also see a new paradigm for exploring the reionization epoch, in the form of 21 cm observations of neutral hydrogen at high redshifts (Chapter X). The Square Kilometre Array (SKA) and the various “pathfinder” projects will be able to both detect HZQs [147] and characterise, in particular, their H II regions [111, 124, 148, 149].

Such data would go a long way to providing a full empirical characterisation of hydrogen in the reionization epoch, although real understanding will only come in the context of theoretical models. The process of reionization is sufficiently complicated that progress here will inevitably come from numerical simulations. At present the available simulations are either fast and global but approximate (e.g., [150, 151]) or more complete but limited to small volumes (e.g., [143, 152, 153]). Inevitable increases in computing power will ensure steady progress, as will the increasingly tight observational constraints that will obviate the need for such a wide range of initial conditions to be considered.

The final step will be bringing observation and theory together, something which has largely been tackled using fairly heuristic methods so far. While somewhat understandable given both the ambiguities in the observational signatures and the large number of unknown parameters in the models, it should become possible to deploy more rigorous methods in the future (e.g., [154]). One apparently fundamental difficulty of using numerical models is that it is often impossible to write down

a useful likelihood function – simply comparing, e.g., the transmission along the line-of-sight to a quasar with one realisation from a numerical simulation will almost always yield a bad fit. One promising option in such situations is approximate Bayesian computation (ABC; e.g., [155, 156, 157]), in which it is sufficient to be able to simulate mock data. In practice it requires the use of cleverly chosen summary statistics (e.g., the mean redshifts and lengths of the dark gaps discussed in Section 5.1), but as long as some information is encoded then rigorous inferences can be made. There is reason to be hopeful that quasar studies of reionization will, over the next decade, evolve from their current exploratory nature to provide rigorous quantitative constraints on the progress of reionization in the early Universe.

Acknowledgements Thanks to Xiaohui Fan, Zoltan Haiman, Chris Hirata, Linhai Jiang, Leon Lucy, Andrei Mesinger, Subu Mohanty, Ashara Peiris, Andrew Pontzen, Steve Warren and Chris Willott for useful discussions about quasars, reionization and the rich physics of the hydrogen atom.

References

1. X. Fan, C. L. Carilli, and B. Keating. Observational Constraints on Cosmic Reionization. *ARA&A*, 44:415–462, sep 2006.
2. S. G. Djorgovski, M. Bogosavljevic, and A. Mahabal. Quasars as probes of late reionization and early structure formation. *NAR*, 50:140–145, March 2006.
3. X. Fan et al. Constraining the evolution of the ionizing background and the epoch of reionization with $z \sim 6$ quasars. II. A sample of 19 quasars. *AJ*, 132:117–136, jul 2006.
4. I. D. McGreer, A. Mesinger, and X. Fan. The first (nearly) model-independent constraint on the neutral hydrogen fraction at $z \sim 6$. *MNRAS*, 415:3237–3246, August 2011.
5. P. J. E. Peebles. *Principles of Physical Cosmology*. Princeton University Press, 1993.
6. J. A. Peacock. *Cosmological Physics*. Cambridge University Press, January 1999.
7. X. Fan, M. A. Strauss, D. P. Schneider, et al. A survey of $z > 5.7$ quasars in the Sloan Digital Sky Survey. II. Discovery of three additional quasars at $z > 6$. *AJ*, 125:1649–1659, apr 2003.
8. R. L. White, R. H. Becker, X. Fan, and M. A. Strauss. Probing the ionization state of the Universe at $z > 6$. *AJ*, 126:1–14, July 2003.
9. J. Greiner et al. GRB 080913 at redshift 6.7. *ApJ*, 693:1610–1620, March 2009.
10. M. Iye et al. A galaxy at a redshift $z = 6.96$. *Nature*, 443:186–188, September 2006.
11. C. Hazard, M. B. Mackey, and A. J. Shimmins. Investigation of the Radio Source 3C273 by the method of Lunar Occultations. *Nature*, 197:1037–+, March 1963.
12. M. Schmidt. 3C 273 : A star-like object with large red-shift. *Nature*, 197:1040–1041, mar 1963.
13. M. J. Rees. Black Hole Models for Active Galactic Nuclei. *ARAA*, 22:471–506, 1984.
14. X. Fan et al. A survey of $z > 5.8$ quasars in the Sloan Digital Sky Survey. I. Discovery of three new quasars and the spatial density of luminous quasars at $z \sim 6$. *AJ*, 122:2833–2849, dec 2001.
15. C. J. Willott et al. The Canada-France High- z Quasar Survey: Nine new quasars and the luminosity function at redshift 6. *AJ*, 139:906–918, March 2010.
16. I. D. McGreer, R. H. Becker, D. J. Helfand, and R. L. White. Discovery of a $z = 6.1$ Radio-Loud Quasar in the NOAO Deep Wide Field Survey. *ApJ*, 652:157–162, nov 2006.
17. R. J. Cool et al. The Discovery of Three New $z > 5$ Quasars in the AGN and Galaxy Evolution Survey. *AJ*, 132:823–830, aug 2006.

18. G. R. Zeimann, R. L. White, R. H. Becker, J. A. Hodge, S. A. Stanford, and G. T. Richards. Discovery of a Radio-selected $z \sim 6$ Quasar. *ApJ*, 736:57, July 2011.
19. D. G. York et al. The Sloan Digital Sky Survey: Technical summary. *AJ*, 120:1579–1587, September 2000.
20. P. Astier et al. The Supernova Legacy Survey: measurement of Ω_M , Ω and w from the first year data set. *A&A*, 447:31–48, February 2006.
21. S. D. J. Gwyn. The Canada-France-Hawaii Telescope Legacy Survey: Stacked Images and Catalogs. *AJ*, 143:38, February 2012.
22. N. Kaiser et al. volume 4836 of *Society of Photo-Optical Instrumentation Engineers (SPIE) Conference Series*, page 154, December 2002.
23. K. W. Hodapp et al. Design of the Pan-STARRS telescopes. *Astronomische Nachrichten*, 325:636–642, October 2004.
24. A. Lawrence et al. The UKIRT Infrared Deep Sky Survey (UKIDSS). *MNRAS*, 379:1599–1617, August 2007.
25. W. Sutherland et al. The Visible and Infrared Survey Telescope for Astronomy (VISTA): Design, Technical Overview and Performance. *A&A*, 575, March 2015.
26. C. J. Willott et al. Four quasars above redshift 6 discovered by the Canada-France High- z Quasar Survey. *AJ*, 134:2435–2450, December 2007.
27. L. Jiang et al. A Survey of $z \sim 6$ Quasars in the Sloan Digital Sky Survey Deep Stripe. I. a Flux-Limited Sample at $z_{AB} < 21$. *AJ*, 135:1057–1066, March 2008.
28. D. J. Mortlock, M. Patel, S. J. Warren, P. C. Hewett, B. P. Venemans, R. G. McMahon, and C. Simpson. Probabilistic selection of high-redshift quasars. *MNRAS*, 419:390–410, January 2012.
29. D. J. Mortlock et al. A luminous quasar at a redshift of $z=7.085$. *Nature*, 474:616–619, June 2011.
30. B. P. Venemans et al. The identification of z -dropouts in Pan-STARRS1: three quasars at $6.5 < z < 6.7$. *ApJ*, 801, February 2015.
31. X.-B. Wu, F. Wang, X. Fan, W. Yi, W. Zuo, F. Bian, L. Jiang, I. D. McGreer, R. Wang, J. Yang, Q. Yang, D. Thompson, and Y. Beletsky. An ultraluminous quasar with a twelve-billion-solar-mass black hole at redshift 6.30. *Nature*, 518:512–515, February 2015.
32. X. Fan et al. A survey of $z > 5.7$ quasars in the Sloan Digital Sky Survey. III. Discovery of five additional quasars. *AJ*, 128:515–522, aug 2004.
33. C. L. Carilli et al. Ionization near zones associated with quasars at $z \sim 6$. *ApJ*, 714:834–839, May 2010.
34. J. D. Kurk et al. Black Hole Masses and Enrichment of $z \sim 6$ SDSS Quasars. *ApJ*, 669:32–44, November 2007.
35. L. Jiang et al. Discovery of eight $z \sim 6$ quasars in the sloan digital sky survey overlap regions. *ApJ*, 149:188, May 2015.
36. E. Bañados et al. Discovery of Eight $z \sim 6$ Quasars from Pan-STARRS1. *AJ*, 148:14, July 2014.
37. C. J. Willott et al. The Canada-France High- z Quasar Survey: Nine new quasars and the luminosity function at redshift 6. *AJ*, 139:906–918, March 2010.
38. C. J. Willott et al. Eddington-limited accretion and the black hole mass function at redshift 6. *AJ*, 140:546–560, August 2010.
39. C. J. Willott et al. Six More Quasars at Redshift 6 Discovered by the Canada-France High- z Quasar Survey. *AJ*, 137:3541–3547, March 2009.
40. B. P. Venemans et al. Discovery of Three $z > 6.5$ Quasars in the VISTA Kilo-Degree Infrared Galaxy (VIKING) Survey. *ApJ*, 779:24, December 2013.
41. A. C. Carnall et al. Two bright $z > 6$ quasars from VST ATLAS and a new method of optical plus mid-infrared colour selection. *MNRAS*, 451, July 2015.
42. S. W. Warren et al. Discovery of six redshift 6 quasars in the UKIRT Infrared Deep Sky Survey. *A&A*, submitted, 2015.
43. G. D. Becker, J. S. Bolton, P. Madau, M. Pettini, E. V. Ryan-Weber, and B. P. Venemans. Evidence of patchy hydrogen reionization from an extreme Ly α trough below redshift six. *MNRAS*, 447:3402–3419, March 2015.

44. C. J. Willott, A. Omont, and J. Bergeron. Redshift 6.4 Host Galaxies of 10^8 Solar Mass Black Holes: Low Star Formation Rate and Dynamical Mass. *ApJ*, 770:13, June 2013.
45. L. Jiang et al. A Survey of $z \sim 6$ Quasars in the Sloan Digital Sky Survey Deep Stripe. II. Discovery of Six Quasars at $z_{AB} > 21$. *AJ*, 138:305–311, July 2009.
46. B. P. Venemans et al. First discoveries of $z \sim 6$ quasars with the Kilo Degree Survey and VISTA Kilo-Degree Infrared Galaxy survey. *MNRAS*, 453:2259, November 2015.
47. S. L. Reed et al. DES J04544448: Discovery of the First Luminous $z > 6$ Quasar from the Dark Energy Survey. *MNRAS*, in press, 2015.
48. X. Fan et al. A survey of $z > 5.7$ quasars in the Sloan Digital Sky Survey. IV. Discovery of seven additional quasars. *AJ*, 131:1203–1209, mar 2006.
49. T. Goto. Discovery of a new high-redshift QSO at $z = 5.96$ with the Subaru Telescope. *MNRAS*, 371:769–771, September 2006.
50. X. Fan et al. Discovery of redshift 6 quasars in SDSS. *AJ*, submitted, 2015.
51. R. Wang et al. Thermal Emission from Warm Dust in the Most Distant Quasars. *ApJ*, 687:848–858, November 2008.
52. B. P. Venemans et al. Detection of Atomic Carbon [C II] $158 \mu\text{m}$ and Dust Emission from a $z = 7.1$ Quasar Host Galaxy. *ApJ*, 751:L25, June 2012.
53. D. J. Mortlock et al. Discovery of a redshift 6.13 quasar in the UKIRT infrared deep sky survey. *A&A*, 505:97–104, October 2009.
54. R. Wang et al. Star Formation and Gas Kinematics of Quasar Host Galaxies at $z \sim 6$: New Insights from ALMA. *ApJ*, 773:44, August 2013.
55. N. Kashikawa et al. The Subaru High- z Quasar Survey: Discovery of Faint $z \sim 6$ Quasars. *ApJ*, 798:28, January 2015.
56. G. B. Rybicki and I. P. dell’Antonio. The time development of a resonance line in the expanding universe. *ApJ*, 427:603–617, June 1994.
57. H.-W. Lee. Asymmetric Deviation of the Scattering Cross Section around $\text{Ly}\alpha$ by Atomic Hydrogen. *ApJ*, 594:637–641, September 2003.
58. C. M. Hirata. Wouthuysen-Field coupling strength and application to high-redshift 21-cm radiation. *MNRAS*, 367:259–274, March 2006.
59. K. R. Lang. *Astrophysical formulae: A compendium for the physicist and astrophysicist*. Springer-Verlag, 1974.
60. E. Alipour, K. Sigurdson, and C. Hirata. The Effects of Rayleigh Scattering on the CMB and Cosmic Structure. *PRD*, 91:083520, April 2015.
61. K. Bach and H.-W. Lee. Accurate $\text{Ly}\alpha$ scattering cross-section and red damping wing in the reionization epoch. *MNRAS*, 446:264–273, January 2015.
62. B. T. Draine. *Physics of the Interstellar and Intergalactic Medium*. 2011.
63. D. J. Mortlock and C. Hirata. The damping wing from neutral hydrogen in the intergalactic medium. *MNRAS*, submitted, 2015.
64. J. Miralda-Escudé. Reionization of the intergalactic medium and the damping wing of the Gunn-Peterson trough. *ApJ*, 501:15–22, jul 1998.
65. V. Weisskopf and E. Wigner. Über die natürliche Linienbreite in der Strahlung des harmonischen Oszillators. *Zeitschrift für Physik*, 65:18–29, November 1930.
66. J. Tudor Davies and J. M. Vaughan. A New Tabulation of the Voigt Profile. *ApJ*, 137:1302, May 1963.
67. T. Tepper-García. Voigt profile fitting to quasar absorption lines: an analytic approximation to the Voigt-Hjerting function. *MNRAS*, 369:2025–2035, July 2006.
68. M. R. Zaghoul. On the calculation of the Voigt line profile: a single proper integral with a damped sine integrand. *MNRAS*, 375:1043–1048, March 2007.
69. J. Schroeder, A. Mesinger, and Z. Haiman. Evidence of Gunn-Peterson damping wings in high- z quasar spectra: strengthening the case for incomplete reionization at $z \sim 6-7$. *MNRAS*, 428:3058–3071, February 2013.
70. A. Songaila. The Evolution of the Intergalactic Medium Transmission to Redshift 6. *AJ*, 127:2598–2603, May 2004.
71. G. B. Field. The Time Relaxation of a Resonance-Line Profile. *ApJ*, 129:551, May 1959.

72. I. S. Shklovskii. Physical Conditions in the Gaseous Envelope of 3c-273. *Astron. Zh.*, 41:801, 1964.
73. P. A. G. Scheuer. A Sensitive Test for the Presence of Atomic Hydrogen in Intergalactic Space. *Nature*, 207:963, August 1965.
74. J. N. Bahcall and E. E. Salpeter. On the Interaction of Radiation from Distant Sources with the Intervening Medium. *ApJ*, 142:1677–1680, November 1965.
75. J. E. Gunn and B. A. Peterson. On the density of neutral hydrogen in intergalactic space. *ApJ*, 142:1633–1641, nov 1965.
76. M. Schmidt. Large Redshifts of Five Quasi-Stellar Sources. *ApJ*, 141:1295, April 1965.
77. P. Madau. Radiative transfer in a clumpy universe: The colors of high-redshift galaxies. *ApJ*, 441:18–27, March 1995.
78. N. Roche, P. Franzetti, B. Garilli, G. Zamorani, A. Cimatti, and E. Rossetti. Detecting the highest redshift ($z > 8$) quasi-stellar objects in a wide, near-infrared slitless spectroscopic survey. *MNRAS*, 420:1764–1778, February 2012.
79. N. R. Tanvir et al. A γ -ray burst at a redshift of $z \simeq 8.2$. *Nature*, 461:1254–1257, October 2009.
80. T.-S. Kim, J. S. Bolton, M. Viel, M. G. Haehnelt, and R. F. Carswell. An improved measurement of the flux distribution of the Ly α forest in QSO absorption spectra: the effect of continuum fitting, metal contamination and noise properties. *MNRAS*, 382:1657–1674, December 2007.
81. K.-G. Lee. Systematic Continuum Errors in the Ly α Forest and the Measured Temperature-Density Relation. *ApJ*, 753:136, July 2012.
82. R. Cen, J. Miralda-Escudé, J. P. Ostriker, and M. Rauch. Gravitational collapse of small-scale structure as the origin of the Lyman-alpha forest. *ApJ*, 437:L9–L12, December 1994.
83. J. K. Webb, X. Barcons, R. F. Carswell, and H. C. Parnell. The Gunn-Peterson effect and the H I column density distribution of Lyman alpha forest clouds at Z 4. *MNRAS*, 255:319–324, March 1992.
84. E. Giallongo, S. D’Odorico, A. Fontana, R. G. McMahon, S. Savaglio, S. Cristiani, P. Molaro, and D. Trevese. The Gunn-Peterson effect in the spectrum of the Z 4.7 QSO 1202-0725: The intergalactic medium at very high redshifts. *ApJ*, 425:L1–L4, April 1994.
85. A. Songaila, E. M. Hu, L. L. Cowie, and R. G. McMahon. Limits on the Gunn-Peterson Effect at Z 5. *ApJ*, 525:L5–L8, November 1999.
86. X. Fan et al. The Discovery of a Luminous Z 5.80 Quasar from the Sloan Digital Sky Survey. *AJ*, 120:1167–1174, September 2000.
87. A. Mesinger and Z. Haiman. Constraints on reionization and source properties from the absorption spectra of $z > 6.2$ Quasars. *ApJ*, 660:923–932, May 2007.
88. A. Mesinger. Was reionization complete by $z \sim 5 - 6$? *MNRAS*, 407:1328–1337, September 2010.
89. R. A. C. Croft. Characterization of Lyman Alpha Spectra and Predictions of Structure Formation Models: A Flux Statistics Approach. In A. V. Olinto, J. A. Frieman, and D. N. Schramm, editors, *Eighteenth Texas Symposium on Relativistic Astrophysics*, page 664, 1998.
90. R. Barkana. Did the universe reionize at redshift six? *New Ast Rev*, 7:85–100, March 2002.
91. A. Songaila and L. L. Cowie. Approaching Reionization: The Evolution of the Ly α Forest from z 4 to z 6. *AJ*, 123:2183–2196, May 2002.
92. I. T. Iliev, G. Mellema, U.-L. Pen, H. Merz, P. R. Shapiro, and M. A. Alvarez. Simulating cosmic reionization at large scales - I. The geometry of reionization. *MNRAS*, 369:1625–1638, July 2006.
93. S. G. Djorgovski, S. Castro, D. Stern, and A. A. Mahabal. On the Threshold of the Reionization Epoch. *ApJ*, 560:L5–L8, October 2001.
94. R. H. Becker et al. Evidence for Reionization at $z \sim 6$: Detection of a Gunn-Peterson Trough in a $z=6.28$ Quasar. *AJ*, 122:2850–2857, dec 2001.
95. P. Paschos and M. L. Norman. A Statistical Analysis of Intergalactic Medium Transmission Approaching Reionization. *ApJ*, 631:59–84, September 2005.

96. K. Kohler, N. Y. Gnedin, J. Miralda-Escudé, and P. A. Shaver. Redshifted 21 cm Emission from the Pre-Reionization Era. II. H II Regions around Individual Quasars. *ApJ*, 633:552–559, November 2005.
97. S. Gallerani, T. R. Choudhury, and A. Ferrara. Constraining the reionization history with QSO absorption spectra. *MNRAS*, 370:1401–1421, August 2006.
98. I. D. McGreer, A. Mesinger, and V. D’Odorico. Model-independent evidence in favour of an end to reionization by $z > 6$. *MNRAS*, 447:499–505, February 2015.
99. R. J. Bouwens et al. Lower-luminosity Galaxies Could Reionize the Universe: Very Steep Faint-end Slopes to the UV Luminosity Functions at $z > 5 - 8$ from the HUDF09 WFC3/IR Observations. *ApJ*, 752:L5, June 2012.
100. S. L. Finkelstein et al. CANDELS: The Contribution of the Observed Galaxy Population to Cosmic Reionization. *ApJ*, 758:93, October 2012.
101. B. Strömgren. The Physical State of Interstellar Hydrogen. *ApJ*, 89:526, May 1939.
102. Z. Haiman. The Detectability of High-Redshift Ly α Emission Lines prior to the Reionization of the Universe. *ApJ*, 576:L1–L4, September 2002.
103. S. R. Furlanetto, A. Sokasian, and L. Hernquist. Observing the reionization epoch through 21-centimetre radiation. *MNRAS*, 347:187–195, jan 2004.
104. P. R. Shapiro and M. L. Giroux. Cosmological H II regions and the photoionization of the intergalactic medium. *ApJ*, 321:L107–L112, October 1987.
105. P. Madau, F. Haardt, and M. J. Rees. Radiative Transfer in a Clumpy Universe. III. The Nature of Cosmological Ionizing Sources. *ApJ*, 514:648–659, April 1999.
106. Q. Yu and Y. Lu. The Strömgren Sphere, the Environment, and the Reionization in the Local Universe of the Highest Redshift QSOs. *ApJ*, 620:31–43, February 2005.
107. P. Madau and M. J. Rees. The Earliest Luminous Sources and the Damping Wing of the Gunn–Peterson Trough. *ApJL*, 542:69–73, oct 2000.
108. R. Cen and Z. Haiman. Quasar Strömgren Spheres Before Cosmological Reionization. *ApJ*, 542:L75–L78, October 2000.
109. R. Barkana and A. Loeb. In the beginning: the first sources of light and the reionization of the universe. *Physics Reports*, 349:125–238, July 2001.
110. J. S. B. Wyithe and A. Loeb. A large neutral fraction of cosmic hydrogen a billion years after the Big Bang. *Nature*, 427:815–817, February 2004.
111. J. S. B. Wyithe, A. Loeb, and C. Carilli. Improved constraints on the neutral intergalactic hydrogen surrounding quasars at redshifts $z > 6$. *ApJ*, 628:575–582, August 2005.
112. Z. Haiman and R. Cen. Constraining Reionization with the Evolution of the Luminosity Function of Ly α Emitting Galaxies. *ApJ*, 623:627–631, April 2005.
113. A. Mesinger and Z. Haiman. Evidence of a cosmological Strömgren surface and of significant neutral hydrogen surrounding the quasar SDSS J1030+0524. *ApJ*, 611:69–72, August 2004.
114. A. Maselli, S. Gallerani, A. Ferrara, and T. R. Choudhury. On the size of HII regions around high-redshift quasars. *MNRAS*, 376:L34–L38, March 2007.
115. A. Maselli, A. Ferrara, and S. Gallerani. Interpreting the transmission windows of distant quasars. *MNRAS*, 395:1925–1933, June 2009.
116. J. S. Bolton, M. G. Haehnelt, S. J. Warren, P. C. Hewett, D. J. Mortlock, B. P. Venemans, R. G. McMahon, and C. Simpson. How neutral is the intergalactic medium surrounding the redshift $z 7.085$ quasar ULAS J1120+0641? *MNRAS*, 416:L70–L74, September 2011.
117. S. Bajtlik, R. C. Duncan, and J. P. Ostriker. Quasar ionization of Lyman-alpha clouds - The proximity effect, a probe of the ultraviolet background at high redshift. *ApJ*, 327:570–583, April 1988.
118. A. Mesinger, Z. Haiman, and R. Cen. Probing the reionization history using the spectra of high-redshift sources. *ApJ*, 613:23–35, September 2004.
119. J. S. Bolton and M. G. Haehnelt. The nature and evolution of the highly ionized near-zones in the absorption spectra of $z \approx 6$ quasars. *MNRAS*, 374:493–514, January 2007.
120. P. C. Hewett and V. Wild. Improved redshifts for SDSS quasar spectra. *MNRAS*, 405:2302–2316, July 2010.

121. F. Walter et al. Molecular gas in the host galaxy of a quasar at redshift z 6.42. *Nature*, 424:406–408, July 2003.
122. S. Cantalupo, C. Porciani, and S. J. Lilly. Mapping Neutral Hydrogen during Reionization with the Ly α Emission from Quasar Ionization Fronts. *ApJ*, 672:48–58, January 2008.
123. M. Kissler-Patig et al. HAWK-I: the high-acuity wide-field K-band imager for the ESO Very Large Telescope. *A&A*, 491:941–950, December 2008.
124. P. Madau, A. Meiksin, and M. J. Rees. 21 Centimeter Tomography of the Intergalactic Medium at High Redshift. *ApJ*, 475:429–444, February 1997.
125. J. Miralda-Escudé and M. J. Rees. Searching for the Earliest Galaxies Using the Gunn-Peterson Trough and the Ly α Emission Line. *ApJ*, 497:21–27, April 1998.
126. A. Maselli, A. Ferrara, M. Bruscoli, S. Marri, and R. Schneider. The proximity effect around high-redshift galaxies. *MNRAS*, 350:L21–L25, May 2004.
127. J. S. Bolton and M. G. Haehnelt. A closer look at using quasar near-zones as a probe of neutral hydrogen in the intergalactic medium. *MNRAS*, 381:L35–L39, October 2007.
128. J. S. B. Wyithe and A. Loeb. Smooth boundaries to cosmological HII regions from galaxy clustering. *MNRAS*, 374:960–964, January 2007.
129. J. S. B. Wyithe, J. S. Bolton, and M. G. Haehnelt. Reionization bias in high-redshift quasar near-zones. *MNRAS*, 383:691–704, January 2008.
130. R. H. Kramer and Z. Haiman. Probing re-ionization with quasar spectra: the impact of the intrinsic Lyman α emission line shape uncertainty. *MNRAS*, 400:1493–1511, December 2009.
131. R. M. Thomas and S. Zaroubi. Time-evolution of ionization and heating around first stars and miniquasars. *MNRAS*, 384:1080–1096, March 2008.
132. D. Crociani, A. Mesinger, L. Moscardini, and S. Furlanetto. The distribution of Lyman-limit absorption systems during and after reionization. *MNRAS*, 411:289–300, February 2011.
133. Z. Haiman. Cosmology: A smoother end to the dark ages. *Nature*, 472:47–48, April 2011.
134. A. Lidz, M. McQuinn, M. Zaldarriaga, L. Hernquist, and S. Dutta. Quasar Proximity Zones and Patchy Reionization. *ApJ*, 670:39–59, November 2007.
135. M. McQuinn, A. Lidz, M. Zaldarriaga, L. Hernquist, and S. Dutta. Probing the neutral fraction of the IGM with GRBs during the epoch of reionization. *MNRAS*, 388:1101–1110, August 2008.
136. A. Mesinger and S. R. Furlanetto. Ly α damping wing constraints on inhomogeneous reionization. *MNRAS*, 385:1348–1358, April 2008.
137. A. Mesinger, A. Aykatalp, E. Vanzella, L. Pentericci, A. Ferrara, and M. Dijkstra. Can the intergalactic medium cause a rapid drop in Ly α emission at $z > 6$? *MNRAS*, 446:566–577, January 2015.
138. M. Patel, S. J. Warren, D. J. Mortlock, and J. P. U. Fynbo. The reanalysis of spectra of GRB 080913 to estimate the neutral fraction of the IGM at a redshift of 6.7. *A&A*, 512:3–?, March 2010.
139. T. Totani, N. Kawai, G. Kosugi, K. Aoki, T. Yamada, M. Iye, K. Ohta, and T. Hattori. Implications for Cosmic Reionization from the Optical Afterglow Spectrum of the Gamma-Ray Burst 050904 at z 6.3. *PASJ*, 58:485–498, jun 2006.
140. R. Chornock, E. Berger, D. B. Fox, W. Fong, T. Laskar, and K. C. Roth. GRB 140515A at z 6.33: Constraints on the End of Reionization From a Gamma-ray Burst in a Low Hydrogen Column Density Environment. *ArXiv e-prints*, May 2014.
141. S. E. I. Bosman and G. D. Becker. Re-examining the case for neutral gas near the redshift 7 quasar ulas j1120+0641. *MNRAS*, 452:1105, September 2015.
142. R. A. Simcoe, P. W. Sullivan, K. L. Cooksey, M. M. Kao, M. S. Matejek, and A. J. Burgasser. Extremely metal-poor gas at a redshift of 7. *Nature*, 492:79–82, December 2012.
143. K. Finlator, J. A. Muñoz, B. D. Oppenheimer, S. P. Oh, F. Özel, and R. Davé. The host haloes of O I absorbers in the reionization epoch. *MNRAS*, 436:1818–1835, December 2013.
144. The Dark Energy Survey Collaboration. The Dark Energy Survey. *ArXiv Astrophysics e-prints*, October 2005.
145. Ž. Ivezić et al. Large Synoptic Survey Telescope: From Science Drivers To Reference Design. *Serbian Astronomical Journal*, 176:1–13, June 2008.

146. R. Laureijs et al. Euclid Definition Study Report. *ArXiv e-prints*, October 2011.
147. J. S. B. Wyithe, A. Loeb, and D. G. Barnes. Prospects for Redshifted 21 cm Observations of Quasar H II Regions. *ApJ*, 634:715–727, November 2005.
148. M. A. Alvarez and T. Abel. Quasar HII regions during cosmic reionization. *MNRAS*, 380:L30–L34, September 2007.
149. S. Wyithe, P. M. Geil, and H. Kim. Imaging HII Regions from Galaxies and Quasars During Reionisation with SKA. *ArXiv e-prints*, January 2015.
150. B. Greig, J. S. Bolton, and J. S. B. Wyithe. Fast, large-volume, GPU-enabled simulations for the Ly α forest: power spectrum forecasts for baryon acoustic oscillation experiments. *MNRAS*, 418:1980–1993, December 2011.
151. A. Mesinger, S. Furlanetto, and R. Cen. 21CMFAST: a fast, seminumerical simulation of the high-redshift 21-cm signal. *MNRAS*, 411:955–972, February 2011.
152. S. Cantalupo and C. Porciani. RADAMESH: cosmological radiative transfer for Adaptive Mesh Refinement simulations. *MNRAS*, 411:1678–1694, March 2011.
153. I. T. Iliev, G. Mellema, K. Ahn, P. R. Shapiro, Y. Mao, and U.-L. Pen. Simulating cosmic reionization: how large a volume is large enough? *MNRAS*, 439:725–743, March 2014.
154. B. Greig and A. Mesinger. 21CMMC: an MCMC analysis tool enabling astrophysical parameter studies of the cosmic 21 cm signal. *MNRAS*, 449:4246–4263, June 2015.
155. S. Tavaré, D. Balding, R. Griffith, and P. Donnelly. Inferring coalescence times from DNA sequence data. *Genetic*, 145:505–518, 1997.
156. J. Pritchard, M. Seielstad, Perez-Lezaun, and M. A. Feldman. Population growth of human Y chromosomes: a study of Y chromosome microsatellites. *Mol. Bio. and Evol.*, 16:1791–1798, 1999.
157. E. Cameron and A. N. Pettitt. Approximate Bayesian Computation for astronomical model analysis: a case study in galaxy demographics and morphological transformation at high redshift. *MNRAS*, 425:44–65, September 2012.